Dissertation
submitted to the
Combined Faculties for the Natural Sciences and for Mathematics
of the Ruperto-Carola University of Heidelberg, Germany
for the degree of
Doctor of Natural Sciences

Put forward by

Diplom-Physicist Franziska Curdt
Born in Göttingen, Germany

Oral examination: January 16, 2013

4Pi Nanoscopy parallelized by line scanning

Referees:

Prof. Dr. Stefan W. Hell
Prof. Dr. Wolfgang Petrich

Kurzdarstellung

Ein hochauflösendes, scannendes Fluoreszenzmikroskop – oder Nanoskop – ermöglicht die Aufnahme von Strukturen, die kleiner sind als die Beugungsgrenze von Licht. Der entscheidende Punkt in Mikroskopiemethoden, die gezielt auslesen, ist das An- und Ausschalten einer Untergruppe von Fluorophoren innerhalb eines Fokalvolumens mit Hilfe verschiedener reversibel schaltbarer optischer Fluoreszenzübergänge. Wenn zudem der effektive Öffnungswinkel verdoppelt wird, wie in einem 4Pi Aufbau, kann die Auflösung in axialer Richtung entscheidend verbessert werden. Ein Aufbau, der 4Pi und die STimulated- Emission-Depletion-Methode (STED) kombiniert, nutzt das STED-Licht durch lokale Felderhöhung sehr effektiv und erzielt bis heute das kleinstmögliche Scan-Volumen. Die Aufnahme der durch das geringe Volumen gewonnenen Information verlangt jedoch kleinere Scan-Schritte und damit eine verlängerte Aufnahmedauer. Ein parallelisierter Ausleseprozess kann diesen Nachteil kompensieren und ist gerade für die 4Pi-STED-Kombination interessant. Mit dem vorgestellten Auslese-Schema kann die Aufnahmedauer gegen die benötigte Auflösung abgewogen werden. In dieser Arbeit ist ein linienparallelisierter 4Pi-STED Aufbau vorgestellt, der erstmalig ermöglicht, mit einem zehnfach parallelisiertem Scan-Volumen im Vergleich zum Konfokalvolumen eines Einzelpunkts, 20 nm große, fluoreszente Nanopartikel mit einer FWHM von ca. 50 nm zweidimensional hochaufzulösen.

Abstract

A superresolution scanning fluorescence microscope – or nanoscope – allows imaging structures smaller than the diffraction limit of light. The principal idea in targeted readout microscopy methods is the on/off-switching of a subset of fluorophores inside the focal volume with the help of different reversible switchable optical fluorescence transitions. If, in addition, the effective numerical aperture is doubled as in a 4Pi optical setup, the resolving power in axial direction of a far field microscope can be significantly increased. Due to the local field enhancement, a 4Pi augmented STimulated Emission Depletion (STED) setup exploits STED light in an effective manner. To this date, it features the smallest effective scannning volume. However, the acquisition of the obtained image information with this slender volume requires smaller scanning steps and in consequence a longer overall acquisition process. This disadvantage can be compensated for by parallel readout and is relevant for a 4Pi-STED combination, in particular. The proposed image parallelization scheme allows to trade-off acquisition speed against required resolution. In this thesis, a 4Pi augmented line parallelized STED setup is presented that is, for the first time, able to resolve 20 nm fluorescent microspheres with a resolution of about 50 nm in two dimensions with a focal volume that is 10 times parallelized as compared to a single spot confocal volume.

Contents

1

Introduction and Motivation

Advances in the exploration of the nanoworld have accounted for immense research progress in the field of microscopy in the last two decades. In particular, the invention and development of fluorescent superresolution microscopy methods in the far field can be considered a breakthrough.

The term superresolution hereby refers to methods that enable the resolution of structures smaller than the Abbe limit of $\Delta x = \frac{\lambda}{2 \cdot NA}$, with Δx denoting the smallest, still resolvable extent, λ the wavelength of the utilized light and NA the numerical aperture of the objective lens [1]. This equation predicts a physical limit for the resolution of an imaging system and has for many decades been thought to be unalterable. For visible wavelengths, this limits the resolution to around 200 nm in lateral and to more than 500 nm in axial dimension.

In the past, resolving smaller features was considered to be possible only for near field methods, or far field methods with wavelengths beyond the visible spectrum. Scanning probe methods such as Scanning Near field Optical Microscopy (SNOM) or Atomic Force Microscopy (AFM) use a fine tip in proximity of a sample to measure the response of different parameters to the tip or the transmitted near field, respectively. These methods can give answers to questions concerning surface topography and appearance. However, deeper lying structures like the interior of cells cannot be assessed by the near field and therefore cannot be imaged with this technique. When using far field techniques that employ electromagnetic radiation of shorter wavelength – like in X-ray microscopy and electron microscopy – other drawbacks are encountered, namely non-specificity, the necessity of vacuum, the impossibility to image samples without special treatment, and the disruptiveness of the measurement to the sample.

Therefore, especially in the field of molecular biology, optical superresolution far field methods are crucial for low invasive investigation of molecular and submolecular structures and sub-surface processes in living samples that have been inaccessible by other imaging techniques. The superresolution methods described in this thesis are based on fluorescence. This means that the samples have to have fluorescent probes and have to be manipulated for this reason. This procedure may influence the sample but, on the other hand, helps to identify and specify discrete structures, organelles, proteins, protein compartments or DNA substructures.

The insertion of fluorescent probes also allows to control the fluorescence within a diffraction limited focal spot. The size of the focus is still diffraction limited but the response of the sample can be manipulated via the control over the number of fluorescent probes within this area. Fluorescent superresolution microscopy techniques can be divided into two categories, techniques with targeted readout and stochastical readout techniques (cf., Fig. 1.1). In principle, both methods aim to restrict the number of fluorescent probes within a diffraction limited focal spot [2].

In stochastic readout methods such as Photo Activated Localization Microscopy (PALM) [3, 4], STochastic Optical Reconstruction Microscopy (STORM) [5], direct STORM (dSTORM) [6], Point Accumulation for Imaging in Nanoscale Topography (PAINT) [7] or Ground State Depletion followed by Individual Molecule return (GSDIM) [8], only an adequate subset of probes are imaged per exposure in a wide field microscope. The mentioned techniques employ different methods to ensure that only a single molecule per diffraction limited area fluoresces within the exposure time. The position of each probe is determined in every single exposure and many exposures are composed to obtain a superresolved image. The subset of probes that are addressed in each exposure is, however, totally random. The advantages of these methods are the comparably low laser intensities and the simple setups. However, aquisition times are in the order of minutes up to hours and artefacts and uncertainties may be introduced by the data post-processing.

The method presented here is based on targeted readout. This means that data

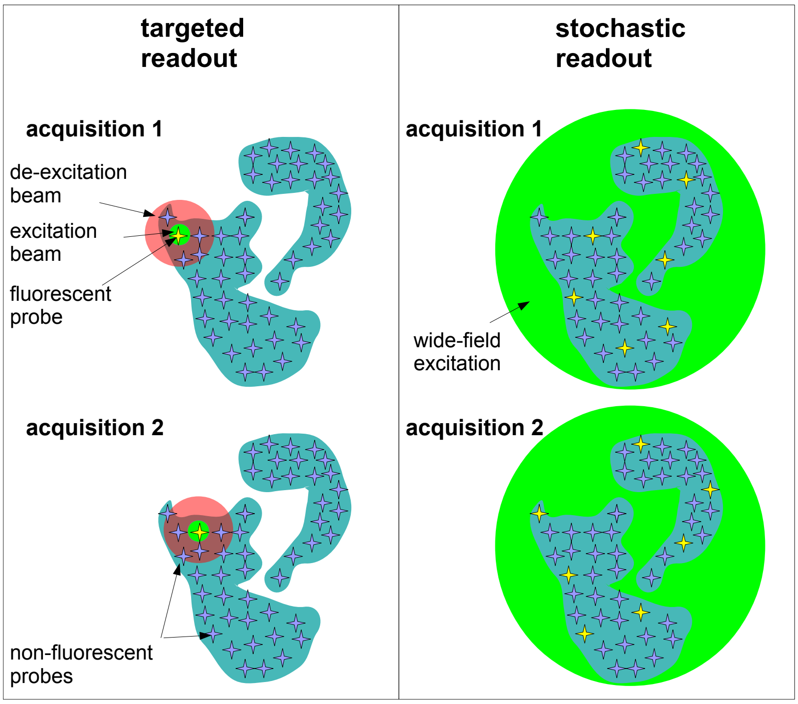

Figure 1.1: Principles enabling fluorescence superresolution. In targeted readout the sample is scanned with an excitation beam and an additional beam that impairs fluorescence in the periphery of the diffraction limited spot (left). In stochastic readout methods, the sample is illuminated wide-field and not more than one molecule per diffraction limited spot must fluoresce for precise localization.

is acquired via a scanning process, in which only a subset of probes are addressed at a targeted point in time and space. This is carried out by controlling the activation or excitation of subsets of fluorophores with so called REversible Saturable OpticaL Fluorescence Transitions (RESOLFT) techniques. In this class of methods fluorescence is excited inside the focal volume via an excitation beam. An additional beam featuring a local intensity minimum close to zero, hereafter referred to as a *zero*, in its center, effectively switches off the fluorescence at all points in the periphery. This elimination of the fluorescent signal can be initiated by stimulated emission or optically switchable dye molecules, such as switchable proteins [9, 10, 11, 12] or organic dyes [13] or by ground state depletion [14].

The most established RESOLFT method today is the Stimulated Emission Depletion [15] method, hereafter referred to as STED. The concepts of any RESOLFT-type microscopes can be exemplified by this method. In a STED setup an additional path for the STED beam is added to a standard scanning microscope. This beam is focused into a torus, also referred to as doughnut-mode, by a phase plate in the back focal plane of the objective lens. It is superimposed with the excitation beam and prohibits fluorescence stemming from outer regions of the diffraction limited light spot. This way, the effective focal volume is decreased and features smaller than the diffraction limit can be discerned. The resolution and the detection point spread function (PSF) – the optical response signal of a point emitter – of the fluorescence signal depend on the power and the shape of the STED PSF and no longer on the size of the diffraction limited confocal PSF. Up to now, effective PSFs with a width of only 5.8 nm have been measured [16], biological samples could be resolved with 15 nm to 20 nm nanometer resolution [17] and superresolved synaptic vesicles have been recorded at video rate [18]. STED has been applied to living cells [19, 20, 21], living tissue samples [22], and it was even possible to image inside living specimen [23].

In a current standard STED microscope, the resolution is typically enhanced only laterally. In the axial dimension resolution is not enhanced, because the STED beam does not feature any on-axis light components in z-direction. With specific phase plates, however, it is possible to focus the STED beam into a pattern that has such axial components. A resolution of down to 110 nm in axial direction has been achieved [24, 25]. The ultimate solution, however, is to use a 4Pi arrangement (cf., Fig. 1.2). In a 4Pi microscope the sample is illuminated through two opposing lenses inside a cavity. The wavefronts of the two lenses are coherently added and the effective solid angle of aperture of the system is doubled. The width of the resulting excitation PSF can be reduced to about 100 nm with sidelobes of less than 5% of the maximum [26]. Combined with STED techniques it is possible to design an effective PSF that is spherical and enables three dimensional superresolution. This concept was shown in principle in 2004 [27, 28] and has been successfully applied in the isoSTED in 2008 [29] with a three dimensional resolution of 40 nm to 45 nm. This is the smallest effective focal volume ever achieved. Its advantage is given by the fact that the focus intensity is enhanced through the interference of the two counter-propagating light fields and high curvature of intensity function at the *zero* along the axial direction. Also in the field of stochastical readout the axial dimension was successfully implemented [30, 31] with 4Pi optics.

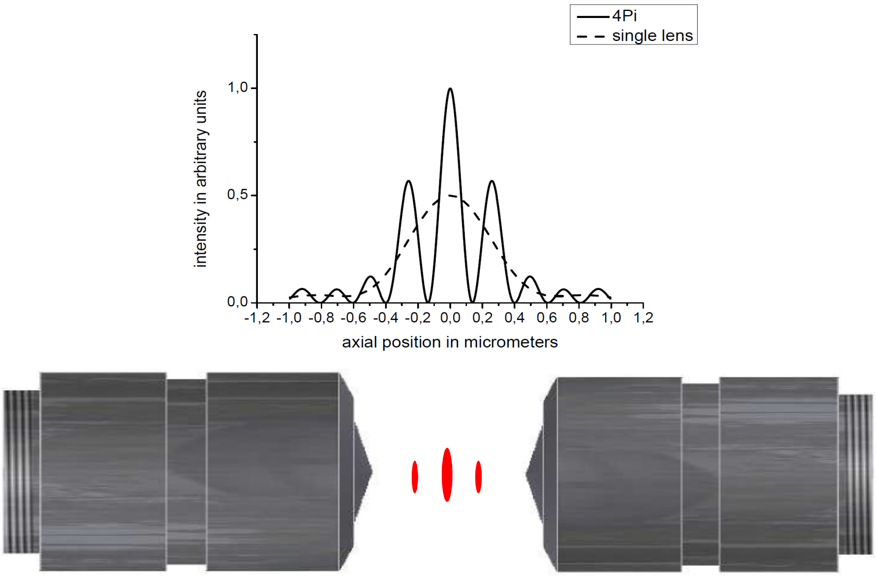

Figure 1.2: 4Pi configuration of two objective lenses. This configuration does not only increase axial resolution, but also enhances local field intensity. This fact makes it interesting for parallelization, in which power needs to be economized, e.g. STED.

For superresolution imaging, the size of the raster increment of the scanning process needs to be decreased to fulfill the Nyquist-Shannon sampling theorem. Yet, decreasing the raster step size leads to increased numbers of pixels. Additionally, the exposure time must be increased to get a sufficient signal-to-noise ratio with the reduced number of molecules per scanned volume. These aspects slow down the acquisition process. To allow high-throughput measurements for biochemical applications, in which measurements need to be repeated in many hundred samples to get a statistically significant result, time becomes a relevant aspect. Fast acquisition is also required to ensure the overall stability of the imaging process and to temporally resolve dynamics, e.g., of living cells. The movement of an object at a speed that is comparable to the scanning speed introduces a spatio-temporal ambiguity that leads to image blur. Additionally, if acquisition takes place on long time-scales (in the order of minutes) it is likely that drift limits image accuracy. Parallelization can reduce the time of the readout process significantly. Since the 4Pi-STED approach has until now achieved the smallest focal volume, a parallelization of this setup is of particular importance.

In order to parallelize, approaches were made using multiple beams. A STED setup with four beams [32] and a 4Pi microscope with up to 16 beams [33, 34] were implemented. However, single-lens STED with multiple beams has a fixed resolution, that is determined by the degree of parallelization and available STED power. In addition, detection with multiple single point detectors is a rather intricate process for a larger number of beams.

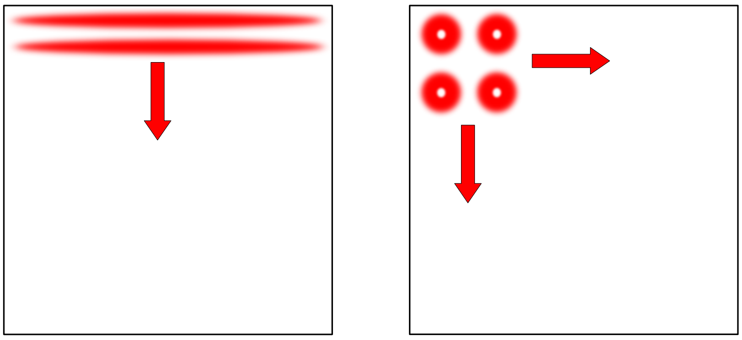

Figure 1.3: Parallelization by line scanning or by multi-focal scanning. In the line scanning approach only one scan direction is needed.

A different approach, which has been pursued in this thesis, is to use a line focus instead of multiple foci. The degree of parallelization can be easier adjusted than in the multi-focal approach and the implementation is comparably simple, moreover the STED pattern is more power efficient. Instead of dividing the beam into various separated beams, that have to be detected individually, the beam is line shaped by a cylindrical lens. Its focal length determines the extent of the focal line (cf., Fig. 1.4). This allows easy modification of the degree of parallelization. Since available laser power is limited, a balance between the degree of parallelization and achievable resolution has to be found. This might depend on the sample and the underlying research goal. For a line focus in a 4Pi setup, various STED illumination patterns can be designed. Using a semi-circle phase plate allows to create a tube-like focus.

For maximal power efficiency it is beneficial to use a pattern with a rather high curvature at the *zero*. In a 4Pi arrangement the intensity profile has axially per se a comparatively high curvature at the minimum. Therefore, to enhance the axial resolution a power of about one fifth compared to the lateral direction is sufficient for comparable resolution. A LabVIEW program, developed in our laboratory, has been employed to calculate possible illumination patterns and to estimate their performance for superresolution.

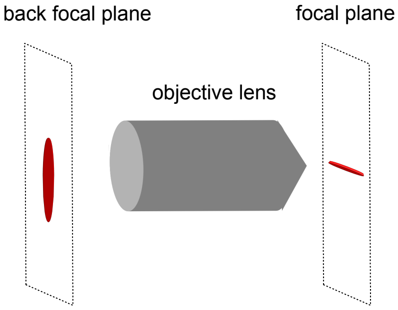

Figure 1.4: A line focus is generated if the back focal plane of an objective lens is illuminated by a line. The line's width in the pupil plane determines its length in the focal plane and can easily be adjusted.

The scope of this work has been the implementation of a 4Pi augmented STED microscope with line illumination. This demanded the design of a cavity, robust enough to minimize perturbations like thermal drift and mechanical instabilities, such as vibrations. As parallelization method, the focus of a cylindrical lens for line shaping and a Charged Coupled Device (CCD) for parallel detection was suggested. In comparison to multifocal microscopy, STED power in a line focus is used more efficiently, because the illuminated area for the same degree of parallelization is smaller. This means that with the same power of the input pulse a larger area can be imaged at the same resolution. However, it has to be taken into account that the resolution along the direction parallel to the line will be left diffraction limited. This can of course be compensated for by imaging the same area several times while turning the line. Also, it should be noted that the focal volume is already two times smaller than for a recent standard STED setup. The advantage is that the second superresolved dimension is axial and therefore perpendicular to the image plane or – in other words – the poorer resolution along the line is compensated for by the resolution improvement in axial direction.

The presented work is based on previous experimental studies done in the field of STED microscopy as well as 4Pi microscopy. Principles and techniques of STED with a titanium sapphire laser of 765 nm and 635 nm excitation have been adopted. The main work has been the design and implementation of a 4Pi microscope from scratch considering experiences made in previous studies, and the development of the first 4Pi line scanning setup. This included the selection of commercially available components, the CAD drawing of parts that had to be machined in the in-house workshop, the further development and modification of a LabVIEW program for the control of alignment axes and their feedback signals, as well as the control of the imaging cycle and camera readout. Finally the performance of the new setup has been evaluated using technical samples.

The thesis is outlined as follows: In the second chapter the basic underlying principles are revisited in brief. Image formation and the impact of diffraction in image formation are considered. The 4Pi concept, meaning the increase of the effective solid angle of aperture by the use of two objective lenses, is explained followed by an introduction to RESOLFT methods. The last part elucidates the principle of phase modulating plates for PSF shaping.

In chapter three, two possible PSFs for line-parallelized 4Pi-STED are considered. Intensity distributions are analysed with emphasis on applicability for RESOLFT and STED in particular. In this respect, the distributions of single polarization components are considered and depletion efficiency for ensembles of fixed, randomly oriented dipole probes is compared for two different STED PSFs.

The design of the setup is presented in chapter four. Stabilization considerations and their implementation are emphasized. The chapter also includes a section about alignment issues.

In chapter five, images obtained with the newly designed setup are shown. The visualization of the systems PSF has been accomplished using technical samples. The performance has been probed with fluorescent microspheres to show resulting resolution enhancement.

Chapter 6 contains the conclusion and discussion and chapter 7 gives an outlook to future work.

2

Basic Concepts

In this chapter underlying principles are introduced. In the first two sections the principle of image formation and PSF shaping are described. The third section comprises the basic 4Pi concept followed by a section that explains STED microscopy. The concepts are summarized in brief and with respect to aspects relevant to this work. A detailed description of the diffraction limited optic can be found in, e.g., [35]. Superresolution concepts are described in [36] and [37], for example.

2.1. Image formation and the diffraction limit

To recognize the relevance of far field fluorescence nanoscopy, the fundamental limit of standard far field microscopes is reconsidered.

Although far field imaging is an unique imaging technique that allows non invasive imaging, it is inevitably affected by diffraction. In the nineteenth century Ernst Abbe [1], Lord Rayleigh [38] and Verdet [39] predicted that this (and not the quality of the optics) physically limits the resolution of lens based optics. In a microscope, even if lenses are of high quality and free of aberration, a point source will be imaged to a diffraction pattern, called Airy pattern. The pattern features a maximum in the center, the Airy disk. A detail that is smaller than the size of this disk will appear blurred. The image of a second emitter should not overlap with its neighbour in a distance smaller than the distance of the minima of the Airy pattern, otherwise their Airy pattern mingle. This restriction, called Rayleigh criterion, limits the resolution of any optical instrument [40].

If the point emitters in closer distance are imaged simultaneously, the sum of the two images is a blurred area and the resolution of the emitters as single points fails. In numbers, this can be expressed by Abbe's equation for the resolution of a microscope, expressed by the FWHM of an imaged point object:

$$\Delta d_{lateral} = 0.51 \cdot \frac{\lambda}{NA}. \tag{2.1}$$

and

$$\Delta d_{axial} = 1.77 \cdot \frac{n\lambda}{NA^2} \tag{2.2}$$

with

$\Delta d =$ FWHM of a point object in lateral and axial direction, respectively,

$\lambda =$ wavelength of light,

$n =$ refractive index of the surrounding medium,

$NA =$ numerical aperture of the objective lens.

Due to the geometry of a lens that focuses light from a solid angle of a spherical cap, the focus is not spherical but elongated axially. Therefore, the axial resolution of a standard microscope is inferior to the lateral resolution.

A PSF can be considered a three dimensional Airy pattern, that determines the response of the imaging system to a point emitter. It can be expressed as a function, h_{sys}. The images, i, can be described mathematically as a convolution of the object with the point spread function of the system, h_{sys}, with the object o,

$$i = h_{sys} * o. \tag{2.3}$$

In a fluorescence microscope the excitation light as well as the emitted fluorescence is diffracted. Therefore, the PSF itself is a product of the excitation PSF, h_{exc}, and the detection PSF, h_{det}.

$$h_{sys} = h_{exc} \cdot h_{det} \tag{2.4}$$

In a confocal microscope the detected PSF, is a convolution of a point spread function of the emission PSF, h_{em}, and a pinhole function, p:

$$h_{det} = h_{em} * p. \tag{2.5}$$

The systems' PSF, then, becomes

$$h_{sys} = h_{exc} \cdot (h_{em} * p)\,. \tag{2.6}$$

In a confocal microscope out of focus light is kept from detection, because is it blocked at the pinhole. Confocal microscopy technique can be considered the standard in laser scanning microscopy and its performance serves as reference value for superresolution techniques.

2.2. The 4Pi principle

In a 4Pi microscope, patented in 1992 [41], the resolution along the axial direction is improved by a factor of up to seven [42, 43, 44, 45]. The resolution is enhanced by coherently adding the counterpropagating fields of two opposing lenses and thus increasing the effective solid angle of aperture of the system to almost 4π. In a 4Pi setup two objective lenses are coherently illuminated inside a cavity that is built of a beam splitter and cavity mirrors (cf., Fig. 2.2). Commonly, the emitted fluorescence light is detected confocally [36].

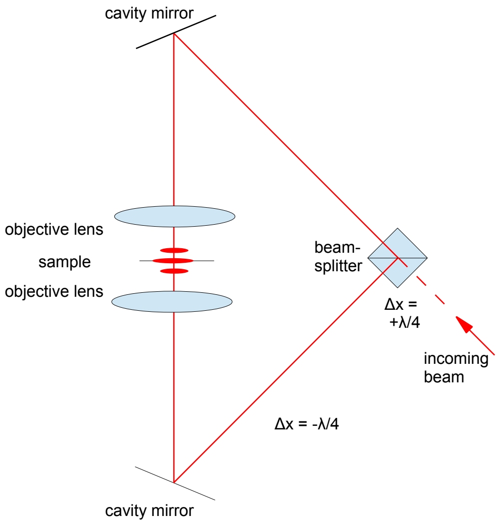

Figure 2.1: Diagram of a 4Pi cavity. The sample is imaged with two objective lenses and two interfering wavefronts. This way the effective solid angle of aperture is doubled. The incoming beam is split into two components that illuminate the two objective lenses coherently. The resulting PSF is an interference pattern of two single lens PSFs.

By definition, a focus is the result of constructive interference of all light components present in the back focal plane. Therefore, the 4Pi focus has the shape of an interference pattern of two single lens confocal PSFs as shown in Fig. 2.2. The resulting PSF typically has the shape of a narrow maximum and a pair of prominent axial sidelobes. They are caused by the vector character of the electromagnetic field at high numerical apertures and the fact, that a number of spatial frequencies will not be transferred. The sidelobes give rise to ghost images. Fortunately these can usually be removed by mathematical post processing as long as their intensity is less than 50%. Since even for objective lenses with high numerical aperture sidelobes range from 60 to 70%, sidelobe suppression techniques such as confocal detection, two-photon excitation [46] and type C interference typically are required. In confocal detection, a pinhole in the detection pathway reduces light emitted from out-of-focus planes and thus the sidelobes.

If two-photon excitation is used, two effects improve axial imaging performance, namely the quadratic dependence of fluorescence on excitation intensity and the use of longer wavelengths with a broader PSF and thus more effective sidelobe suppression by the pinhole. Type C interference means that not only the excitation, but also the fluorescence light interferes. Because of the difference in wavelength, the sidelobe position is shifted and the resulting PSF has a very narrow maximum with suppressed sidelobes (cf., Fig. 2.3). Concerning light at the focus or emitted from the focus, only one reflection at the beam splitter takes place for one cavity arm. The phase difference between the reflected and the transmitted beam at the beamsplitter is $\frac{\pi}{2}$. For constructive interference an additional phase shift of -$\frac{\pi}{2}$ (a length shift of -$\frac{\lambda}{4}$) needs to be added in the non reflected light path.

The focus of each objective lens can be calculated with the integral representation of the diffracted fields, following Richard and Wolfs [47]. At a distance of the lens, where near field components can be neglected, the field at a point $\vec{r} = (r, \theta, \phi)$ with respect to the focus is given by:

$$\vec{E}(\vec{r}) =$$

$$\frac{ifl_0}{\lambda}\begin{pmatrix} -\int\limits_0^{\alpha}\int\limits_0^{2\pi}\sqrt{\cos\theta'}\cdot\sin\theta'\cdot\Big(\cos\theta' + (1-\cos\theta')\cdot\sin^2\phi'\Big)\cdot e^{ikr\cos\epsilon}\mathrm{d}\theta'\mathrm{d}\phi' \\ \int\limits_0^{\alpha}\int\limits_0^{2\pi}\sqrt{\cos\theta'}\cdot\sin\theta'\cdot(1-\cos\theta')\cdot\cos\phi\sin\phi\cdot e^{ikr\cos\epsilon}\mathrm{d}\theta'\mathrm{d}\phi' \\ \int\limits_0^{\alpha}\int\limits_0^{2\pi}\sqrt{\cos\theta'}\cdot\sin^2\theta'\cdot\cos\phi'\cdot e^{ikr\cos\epsilon}\mathrm{d}\theta'\mathrm{d}\phi' \end{pmatrix} \tag{2.7}$$

with

$$\begin{aligned} cos\epsilon &= cos\theta\cos\theta' + \sin\theta\sin\theta'\cos\Big(\phi'-\phi\Big) \\ f &= \text{focal length of the lens} \\ l_0 &= \text{amplitude factor} \\ \alpha &= \text{half aperture angle} \\ \lambda &= \text{wavelength of light} \\ n &= \text{refractive index of immersion} \\ k &= \text{wave number.} \end{aligned}$$

The PSF $h(\vec{r})$ is calculated by

$$h(\vec{r}) = \left|\vec{E}(\vec{r})\right|^2. \tag{2.8}$$

For 4Pi, the excitation PSF, h_{exc}, is a superposition of two equal excitation fields, $\vec{E}_{exc}(\vec{r})$, that are counterpropagating,

$$h_{exc}(\vec{r}) = \left|\vec{E}_{exc}(\vec{r}) + M\vec{E}_{exc}(M\vec{r})\right|^2, \tag{2.9}$$

with[1]

$$M = \begin{pmatrix} 1 & 0 & 0 \\ 0 & 1 & 0 \\ 0 & 0 & -1 \end{pmatrix}. \tag{2.10}$$

This equation 2.9 supposes that the two opposing fields have the same phase. This

---

[1] The factor -1 in M accounts for the counterpropagation in z direction.

constructive PSF (cf., Fig. 2.2) has a sharp maximum and 60% sidelobes[2] if the lengths of the two light paths differ by a multiple of the wavelength plus an additional shift of $-\frac{\lambda}{4}$ to compensate for the reflection at the beam splitter cube. Other types of possible PSFs can be achieved by extending the length of one arm and thus adding a phase difference. However, the constructive PSF is the most relevant, because it has only one narrow global maximum and can be deconvolved if sidelobe intensity is sufficiently low. For a total phase difference of π, the result will be a destructive PSF. If the emitted light also interferes at the beamsplitter, the resulting PSF will be modulated. The width of the central peak is further decreased and the sidelobes intensity is below 30% (cf., Fig. 2.3). The total PSF is the product of the excitation PSF, h_{exc}, and the detection PSF, h_{det}.

$$h(\vec{r}) = h_{exc}(\vec{r}) \cdot h_{det}(\vec{r}) \tag{2.11}$$

This yields:

$$h(\vec{r}) = \left|\vec{E}_{exc}(\vec{r}) + M\vec{E}_{exc}(M\vec{r})\right|^2 \cdot \left|\vec{E}_{exc}(\vec{r})\right|^2 * d(\vec{r}). \tag{2.12}$$

If the fluorescence light also interferes constructively, the resulting PSF becomes:

$$h(\vec{r}) = \left|\vec{E}_{exc}(\vec{r}) + M\vec{E}_{exc}(M\vec{r})\right|^2 \cdot \left|\vec{E}_{exc}(\vec{r}) + M\vec{E}_{exc}(M\vec{r})\right|^2 * d(\vec{r}). \tag{2.13}$$

4Pi microscopy allows three dimensional imaging of biological samples and has been successfully combined with RESOLFT [29] and stochastic readout methods [30, 31]. Parallelized imaging has been carried out in Multispot Multiphoton Microscopy (MMM) [33, 48, 34].

---

[2] Sidelobe intensity depends strongly on the aperture of the objective lenses. High aperture lenses of NA = 1.44 are assumed.

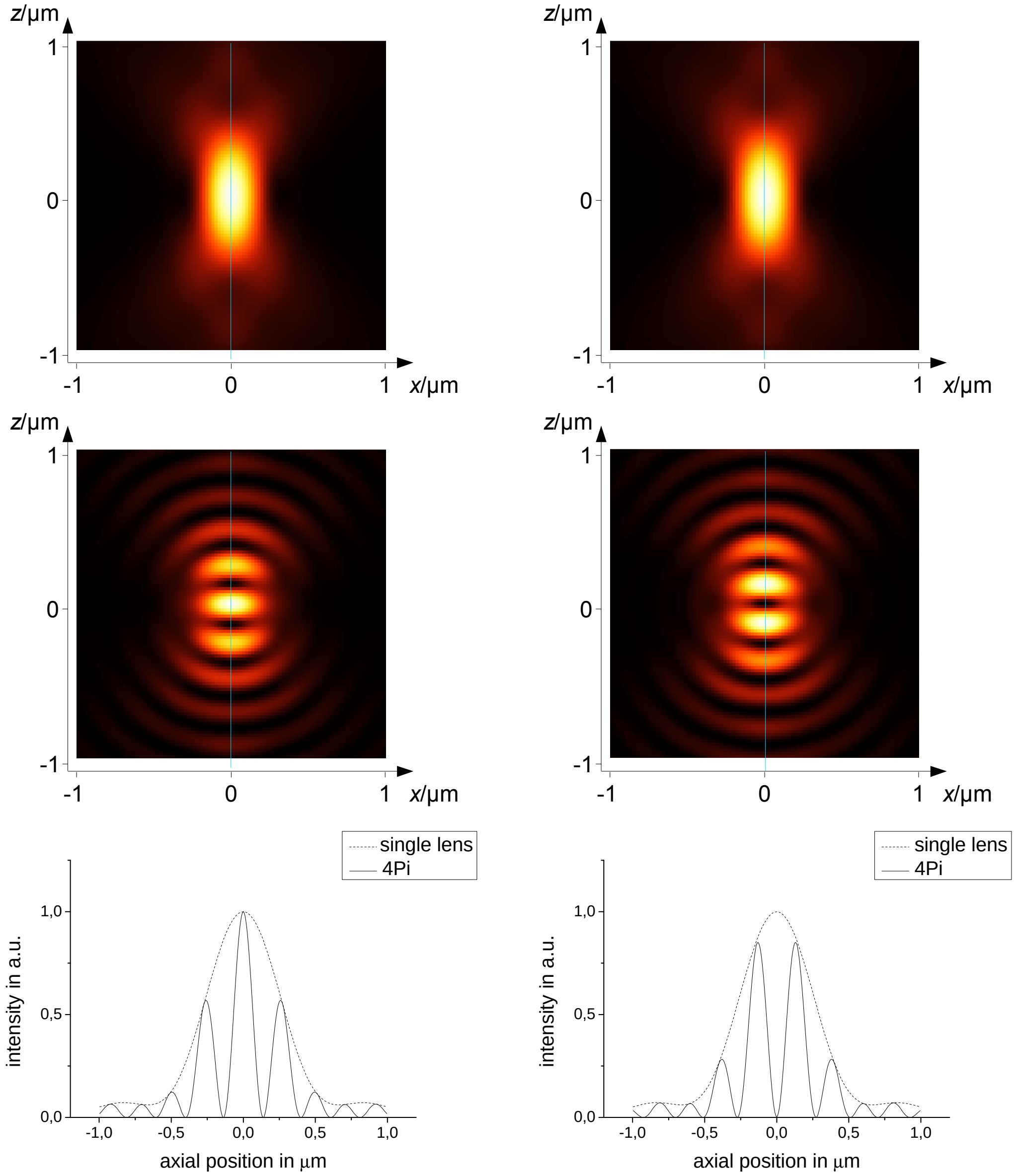

Figure 2.2: An axial 4Pi excitation PSF in comparison to a PSF of a single lens. The main central maximum of the PSF is in the order of 5 times smaller than the PSF of a single lens. The interference pattern changes in dependence on the relative phase difference of the interfering beams. Shown are the constructive case (left) and the destructive case (right) for excitation at 635 nm.

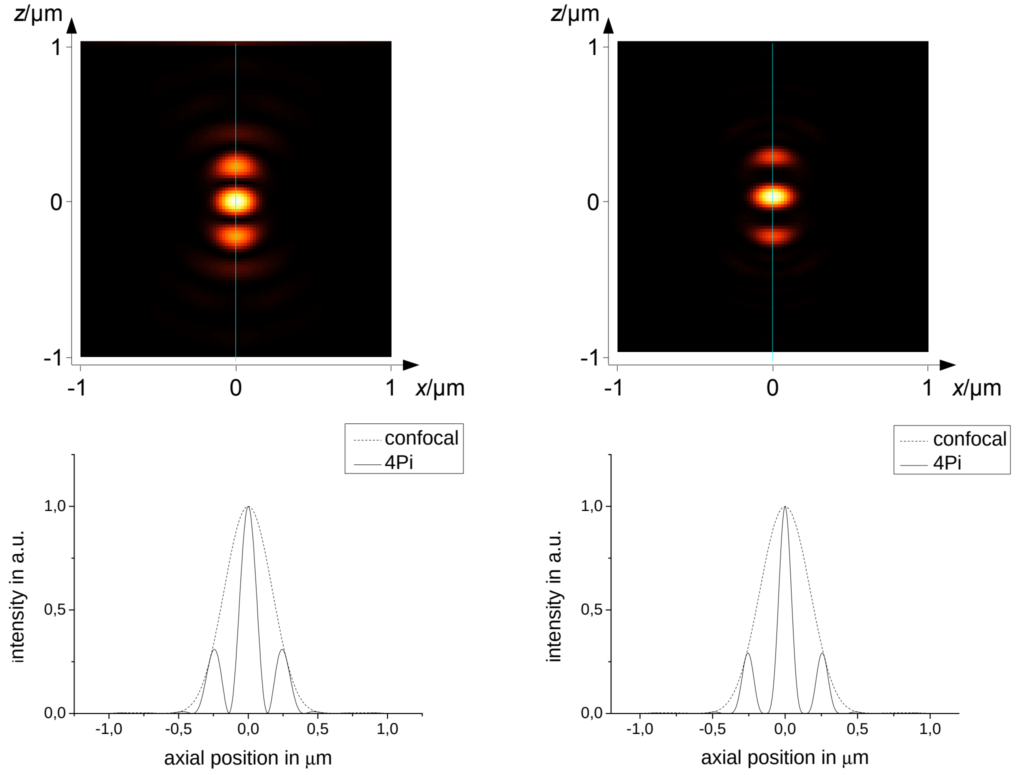

Figure 2.3: 4Pi PSF calculated for an excitation wavelength of 635 nm and fluorescence emission at 660 nm. If only the excitation light interferes and the fluorescence light is detected confocally, the PSF is called type A (left). In type A configuration the FWHM of the central peak is 140 nm and the sidelobes intensity is 30% of the maximum. If the excitation light and the fluorescence light interfere and have the same phase, the PSF is called 4Pi type C (right). Here, the FWHM is only 100 nm. In this case, sidelobes are below 30%.

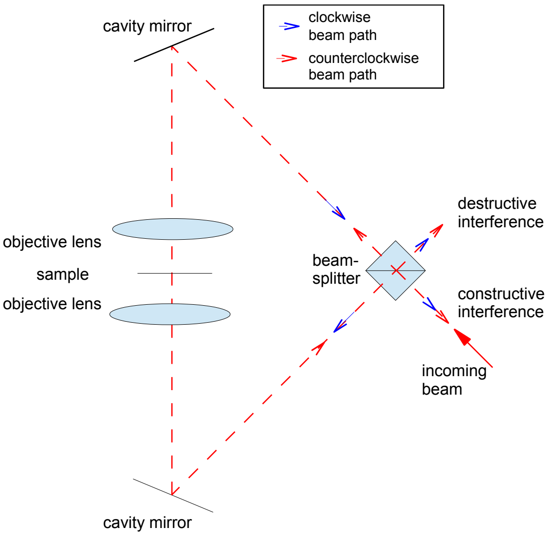

Figure 2.4: Diagram of a 4Pi cavity for the transmitted light. The incoming beam is split into two components that travel through the cavity in opposite direction as indicated with blue and red arrows. The exiting beams are constructively interfering at the entrance side and destructively interfering at the other side of the beamsplitter. The transmission interference is used for alignment control. Misalignment of the foci leaves the interference incomplete. The observed interference pattern in the pupil plane indicates details of lateral displacement.

Not directly relevant for the image, but an indication for alignment, is the consideration of the light that is transmitted through the cavity.

Considering the cavity for light that is passing through, it acts as a Sagnac type interferometer (cf., Fig. 2.4). Light that returns to the incoming light path is interfering constructively, whereas light that leaves the cavity at the other side is interfering destructively. This is due to the fact that any reflection at a 50% beamsplitter introduces a phase shift of $\frac{\pi}{2}$[3]. Therefore, in the first case light passing the cavity clockwise as well as counterclockwise experiences a total phase shift of $\frac{\pi}{2}$, the difference is zero resulting in constructive interference. In the second pathway, light passing clockwise is not reflected at the beamsplitter, whereas light passing counterclockwise is reflected twice. So in this case the total phase difference is π resulting in destructive interference. This phenomenon can be used for alignment check, because misalignment of the two foci will result in an incomplete interference of the counterpropagating fields at the beamsplitter.

---

[3] The additional phase shift of π at each silver mirror result in a total phase shift of 2π. This effect is symmetrical for both cavity arms and thus irrelevant for the argumentation.

2.3. STED principle

The RESOLFT method STED was first proposed by Hell [15] and implemented by Hell and Klar [49] later in the nineties. It is the most prominent targeted readout nanoscopy method and yields the highest resolution up to present.

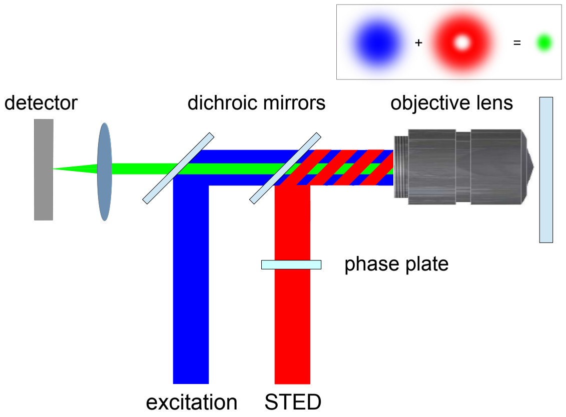

Figure 2.5: Diagram of a typical STED setup. The excitation and the STED beam depicted in blue and red are merged at a dichroic mirror. The STED beam is shaped into a torus via a phase plate. The excitation light stemming from the central area that is not depleted by the STED beam is collected by a point detector.

The hallmark of STED is to address only a subset of fluorescent probes inside a diffraction limited excitation spot. In other words, to define the position of a fluorescent molecule at a given point, r_i, fluorescence of molecules in close distance to this point has to be kept from fluorescing at the same time and the same wavelength to make sure that the given signal stems from a small region, $r_i + \Delta r$, with $\Delta r << \frac{\lambda}{2}$. This way, probes inside a diffraction limited spot can be sequentially mapped. The decisive point is to have at least two different states of the molecule, one which is fluorescent and one which is not. In STED these states are given by the energy levels of the dye molecule. In the classical view, electrons in the excited state cause spontaneous fluorescence when returning to the ground state. To avoid this fluorescence, a competing transition must outperform spontaneous emission. This is achieved by stimulated emission. The emitted fluorescence caused by stimulated emission is of the same wavelength as the STED beam and is separable from the spontaneous fluorescence signal.

Let $k_{depl} = \sigma I(r)$ (with the STED intensity, I, and optical cross section of the transition, σ) denote the rate of fluorescence depletion by stimulated emission, then there is a saturation intensity, $I_{sat} = (\sigma \cdot \tau_{fl})^{-1}$, that is high enough to deplete half of the fluorescence. With fluorescence lifetimes of typically 10^{-9} s and an optical cross section of 10^{-16} cm^2 this yields saturation intensities in the order of $3 \cdot 10^{25}$ photons/cm^2 or 10 MW/cm^2.

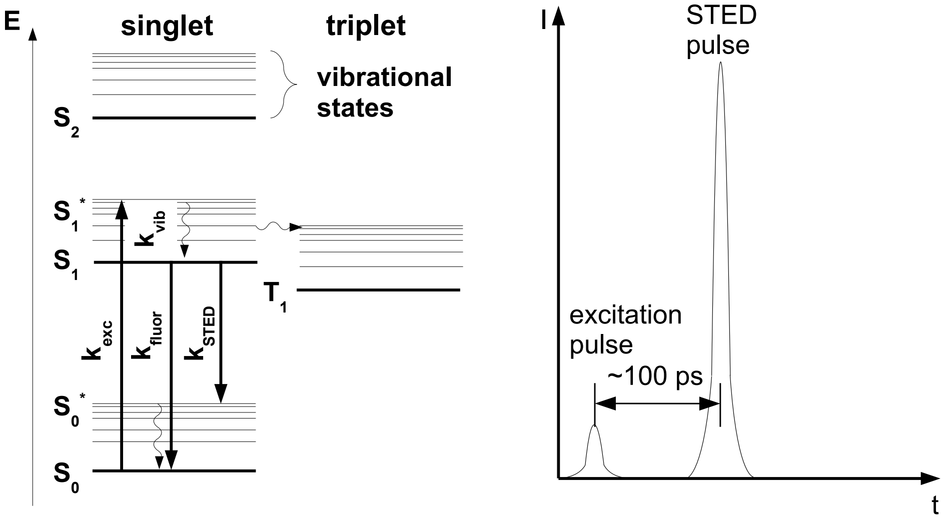

Figure 2.6: A Jablonski diagram (left) displays the molecular transitions that are involved in STED. The rates k can be described in the classical view by means of rate equations that yield exponential characteristics Fluorescence is excited to a vibrational state S_1^* with the rate k_{exc}, that almost immediately decays to S_1 with k_{vib}. A STED photon stimulates the decay of S_1 to S_0^* with k_{STED}. Re-excitation by the STED beam is small because S_0^* decays rapidity to S_0 at rate k_{vib}. Fluorescence takes place at a rate k_{fluo}. The pulse sequence is shown (right). The excitation pulse is followed by the STED pulse after about 100 ps. For high STED energies spontaneous emission is predominant and practically no fluorescence occurs.

In a typical STED setup, (cf., Fig. 2.5) the excitation beam is merged with the STED beam via a dichroic mirror. The STED beam is phase modulated with a phase plate such that it is focused into a torus instead of a point focus. In a pulsed STED setup the excitation pulse is followed – after about 100 ps – by a STED pulse of a few hundred picoseconds. This way, photons are absorbed and the molecule is in an excited state. After vibrational relaxation that occurs immediately, the STED pulse implies stimulated emission. The STED beam is red-shifted in wavelength and thus should not be able to re-excite electrons in the ground state (cf., Fig. 2.6).

The STED beam features a local intensity minimum in its center. All fluorescence in the periphery of the center will be hampered and the remaining fluorescent signal stems from a significantly smaller spot with a diameter, Δr, of

$$\Delta r \approx \frac{\lambda}{2 \cdot n \cdot \sin\alpha \cdot \sqrt{1+\frac{I_{max}}{I_{sat}}}} \tag{2.14}$$

with

$\lambda =$ wavelength of fluorescence light

$n =$ refractive index of immersion

$\alpha =$ semiaperture angle

$I_{max} =$ peak intensity of the STED beam

$I_{sat} =$ saturation intensity.

This effective PSF determines the extent of the smallest still resolvable object. The resolution is no longer limited by diffraction but can be significantly enhanced [50], [51], [52]. The size of the effective PSF and thus the resolution of the microscope depends on the intensity of the STED beam. Only the part of the area in which the STED light has an intensity above I_{sat} is effectively switched off. The resolution scaling is shown in Fig. 2.7 [53]. It is also possible to do STED with continuous wave (CW) lasers. Here, no synchronisation is required. However, as excitation and

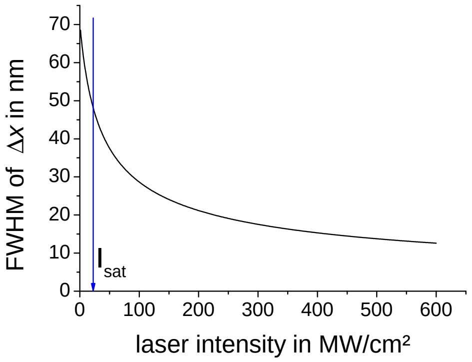

Figure 2.7: Resolution in dependence on STED power [53].

depletion processes are concurring, average intensities that are approximately five times higher than for pulsed STED are needed to achieve the same resolution [54].

2.4. PSF shaping with phase plates

For RESOLFT type methods the creation of *zeros* becomes necessary. A *zero* is a local intensity minimum in the center of an illumination pattern used for off-switching.

A possibility to alter the shape of a beam and its focus is to introduce phase shifts to parts of the field components in the pupil plane. This is achieved with the help of phase plates placed in the back aperture, that have particular structures. A variety of phase patterns can be created. Here, the two most important ones for RESOLFT microscopy, the vortex phase plate and the one used in the presented setup, the semi-circular phase plate, are discussed.

Today, in the majority of STED setups a beam with an optical vortex is used. This is a point singularity in a field distribution of a light field propagating in a screw-like manner. The phase gradient direction of these fields is swirled around the center. The light intensity in this singularity is zero [55]. Such a field can be created using circular polarized light. A vortex phase plate is used (c.f., Fig. 2.8 to add the characteristic phase gradient. The phase shifts increase linearly from 0 to 2π around the center of the phase plate, such that the resulting beam features a vortex. Focused by a lens, the intensity distribution resembles a doughnut.

In this work a semi-circular phase plate was used. Here, the circular area of the phase plate can be divided into two semi-circles. One half of the phase plate adds zero phase shift and the other one a phase shift of π. This phase shift results in a PSF that features two intensity maxima as shown in Fig. 2.8. The *zero*, however, is not rotationally symmetric. Note, that polarization components perpendicular to the border of the two semi circles will give rise to z-polarized intensity components in the center of the focus. In a single-lens RESOLFT setup, light needs to be linear polarized parallel to the border of the semi circles.

For RESOLFT microscopy image quality depends strongly on the quality of the *zero*. Any remaining light components deplete the signal and impair the signal-to-noise ratio. When STED power is increased to achieve a smaller effective PSF,

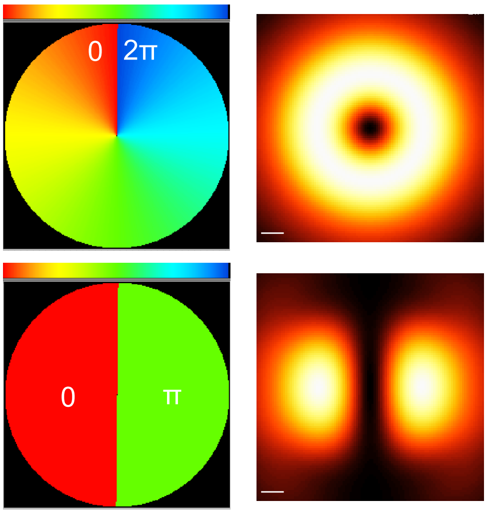

Figure 2.8: Phase plate (left) and resultant foci (right). The vortex plate (top), needs to be illuminated with circular light and the semi-circular phase plate (bottom) with linear polarized light. For the semi-circular phase plate, the polarization vector needs to be parallel to the semi circles' border. The scale bar is 100 nm.

remaining fluorescence signal may become too weak for detection. This limits the employable STED power. In consequence, the resolution can not be increased over a certain value if the *zero* is not perfect.

Semi-circular phase plates are produced by vapor deposition of dedicated minerals, eg. MgF_2 or Cryolite onto glass substrates in a structured manner.

2.5. Photo detectors

The image quality of a microscope depends not only on excitation optics but in addition on efficient detection. Therefore, a choice of detectors and their characteristics are revisited in brief. For scanning fluorescence microscopy usually point detectors are used. These are primarily photon multiplier tubes (PMT) or semiconductor based detectors such as avalanche photo diodes (APD). For parallelized detection charged coupled devices (CCDs) and especially electron multiplying charged coupled devices such as (EMCCDs) are used. APD array detectors are available, however they do not yet offer the same sensitivity as EMCCDs and suffer from low fill factors. PMTs are vacuum tubes, that consists of a photosensitive cathode, an

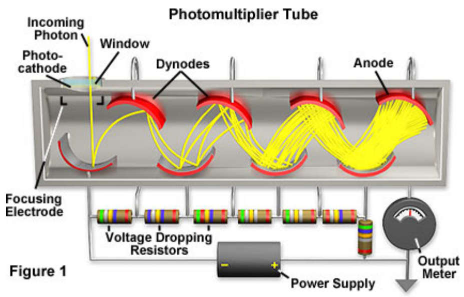

Figure 2.9: Artist view of a photomultiplier tube [56].

electron multiplier and an anode. Photoelectrons are released into the vacuum tube when photons hit the cathode. They are focused onto a cascade of dynodes, where they are multiplied stepwise. A sharp current pulse caused by the incident photon is then detected at the anode. Photomultiplier feature high amplification factors, however their quantum efficiency is rather low, especially for longer wavelength (on the order of 20%). However, their gain can be adjusted dynamically via the applied voltage. APDs use the avalanche effect in semiconductors for sensitive single photon detection. They have high quantum efficiency (up to 90%), but lower amplification factors (500-1000)[4]. They consist of a pn-layer, like a standard photo diode and an additional p layer that acts as a multiplication zone. Photons are absorbed in

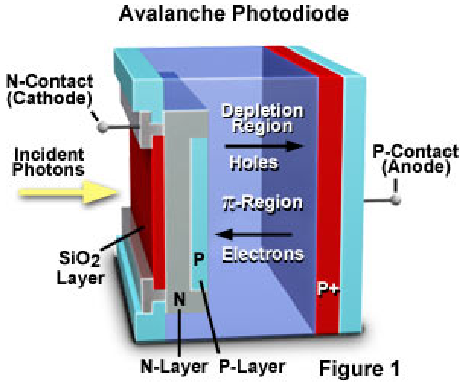

Figure 2.10: Artist view of an avalanche photo diode [57].

---

[4] In Geiger-Mode a single photon count can be amplified with a gain of 10^6. The detector is used for single photon counting, but can not amplify optical signals linearly.

the depletion zone and electrons are accelerated towards the pn-junction, were they induce an avalanche of charges.

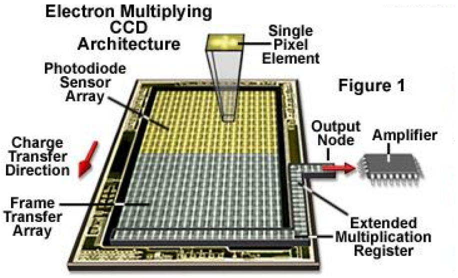

Figure 2.11: Artist view of an EMCCD[58].

CCDs detect photons not only from a point, but a whole area of photo diodes. The principle is to shift charges inside an array and readout a sequence that can be allocated to the pixels. Each pixel acts as light sensitive capacitor, that collects electric charges generated in the photo sensitive semiconductor layer. Applying a positive voltage at the adjacent pixel leads to a charge transfer towards this pixel. By shifting the charges pixel by pixel the array can be readout sequentially. In an EMCCD, an additional gain register provides single photon detectability. Here, electrons are multiplied via impact ionization. This enables high electron gains (on the order of 1000). The readout noise is very low on the order of 1/100 photons per pixel.

For parallel detection an EMCCD to date provides the best performance for parallel readout.

3

Parallelization Concepts

In the first part of this chapter the line parallelization concept is introduced and compared to alternative approaches. Moreover, potential STED PSFs and the theoretical resolution enhancement are presented.

3.1. State of the art

The reduction of the effective detection volume in superresolution targeted readout methods will increase the number of scanning steps. Additionally, due to the smaller detection volume the signal strength is reduced. Consequently, image acquisition will take longer.

A slow imaging process has several disadvantages. On top of the excessive time needed for high throughput applications, it results in insufficient temporal resolution of dynamic processes and susceptibility to system instabilities like mechanical drift or vibrations. To counteract these effects, it is necessary to parallelize the scanning process. However, the following aspects need to be considered. First of all, the parallelization should not affect the quality of the image. Therefore, the introduction of aberrations and inhomogeneities should be avoided. In addition, laser power should be economized for STED, since it determines the achievable resolution.

In the past a number of parallel scanning microscopes have been developed, especially in the field of single-photon confocal and two-photon confocal microscopy [59], but also in 4Pi [34] and STED microscopy [32]. Most of them involve multiple foci. Multiple foci can, e.g., be generated by using a number of beam-lets, a pattern

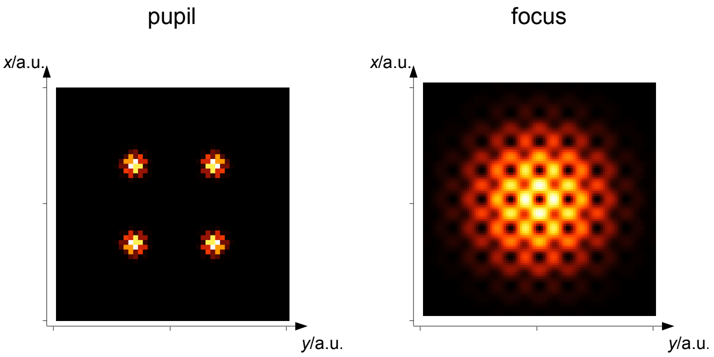

Figure 3.1: Multi foci pattern for 4 spots in the back focal plane. The back focal plane illumination signal (left) and the resulting pattern with multiple *zeros* in the focal plane is shown.

illumination or microlens array illumination.

In the beam-let methods, the scanning beam is divided into several sub-beams with the help of standard optical elements like a cascade of mirrors [60], [61] or birefringent crystals [34], [32]. Here, the single sub-beams illuminate the entire entrance pupil at a slightly tilted angle and the single foci are correspondingly shifted in the image plane. The drawbacks are the complexity of the setup for higher degrees of parallelization and the fact that the density of the resulting illumination pattern is restricted. If the illumination spots are generated in a very close distance, crosstalk may influence STED performance.

In patterned illumination only parts of the back aperture are illuminated coherently. In this way, very dense patterns can be generated. Fig. 3.1 shows an example of a STED pattern for four illumination spots with certain phase offsets. The intensity distribution, however, tends to be rather inhomogeneous. A more homogeneous pattern is proposed in [62] and shown in 3.2. The drawback of such an approach is the relatively high power loss.

Alternatively, a microlens array is used to focus one beam into multiple foci [59], [63], [64]. Here, aberrations and intensity inhomogeneities limit their performance, because the single lenses in an microlens array have a rather low degree of correction.

So far 4Pi microscopy was successfully parallelized using birefringent crystals in a Multi-focal Multiphoton Microscopy (MMM) setup [34]. The crystal separates the different polarization components into two beams. By using a stack of n Wollaston

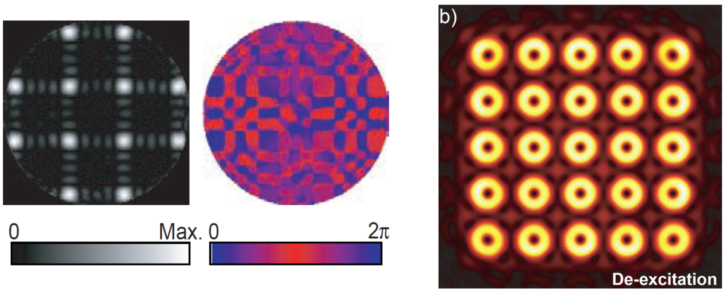

Figure 3.2: Uniform Multi-foci pattern with modulated pupil function. Amplitude and phase distribution of the pupil function (left) and the resulting pattern in the focal plane (right) [65].

prisms the number of beams can be increased by a factor of 2^n. A multi-focal STED setup was successfully implemented for $n = 2$ [32]. Advantages of this approach are the modest power loss and the avoidance of optical aberrations. However, the beams have to have a certain distance from each other, which limits the degree of parallelization. In addition, parallel confocal detection can be intricate.

3.2. Line scanning

A straight forward method to achieve a high degree of parallelization is to scan with a line focus. It permits confocal detection at least in one dimension and requires only one dimensional, namely, lateral scanning. Thus, acquisition speed can be increased significantly. A line focus can be rendered with the help of a cylindrical lens that focuses light in only one dimension. Imaging such a line focus to the back focal plane of an objective lens yields a focus for the collimated dimension and a wide-field illumination for the other one. The result of a line-shaped illumination with constant phase in the back focal plane is a line focus as depicted in Fig. 1.4. The width of the line in the back focal plane, given by the focal length of the cylindrical lens, determines the length of the line focus. Parallel line detection is achieved with an EMCCD camera, where just a few lines of pixels on the chip are read out.

For superresolution, a line-shaped *zero* needs to be generated. For a single lens microscope, resolution is enhanced in only one dimension, whereas in a 4Pi setup the axial direction can be included. The result is an illumination pattern that enables

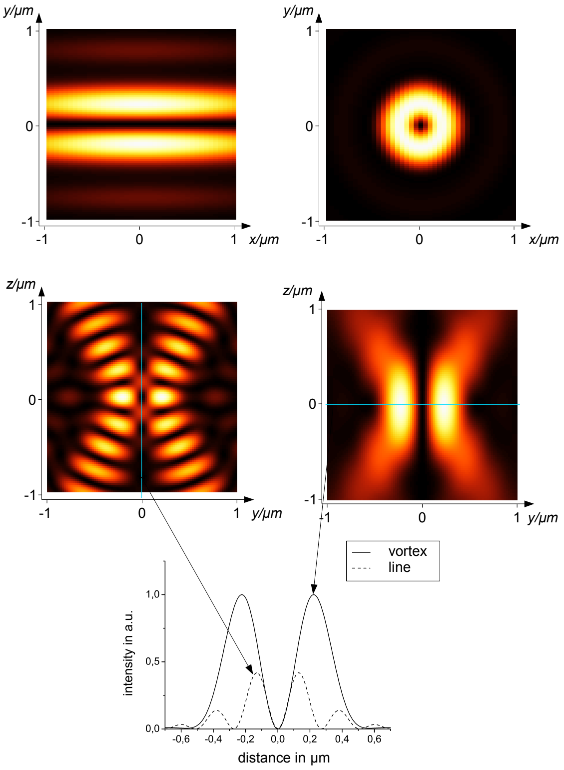

Figure 3.3: Comparison of a line shaped 4Pi PSF (left) versus a point STED PSF (right). The upper row shows the lateral direction and the lower row the axial direction. The direction of potential two dimensional superresolution lies in the xy-plane for the point PSF and in the zy-plane for the line PSF.

two dimensional superresolution. If the line is orientated along the x-direction, the image can be scanned in y-direction and in z-direction. The superresolved plane, however, is the yz-plane as shown in Fig. 3.3. Although the dimension along the line is not superresolved, the focal volume is smaller than in a standard STED setup with a PSF generated by a vortex phase plate. The 4Pi PSF features a very narrow curvature at the *zero* in axial direction. This aspect enables effective depletion at lower peak intensities (cf. Fig. 3.3). Additionally, the line can be rotated to extend superresolution to the third dimension. This way a three dimensional superresolved image can be acquired with a parallelized scan.

A semi-circle phase plate can be employed to achieve a double focus with an one dimensional *zero*. When the back focal plane is illuminated with a line, the focus is shaped to a double line (c.f., Fig. 3.4). Among different possible PSFs, two scenarios have been considered for the setup. One uses a single STED beam and light linear polarized along the line in the back focal plane and in the second approach a combination of two STED beams and circular polarized light is used.

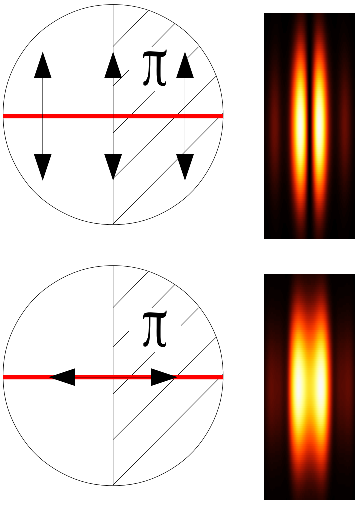

Figure 3.4: Line illumination of a semi-circle phase plate (left). Illuminated areas are red. The black arrow depicts the polarization state of the linear polarized beam. In the right half of the phase plate a phase shift of π is introduced to the incoming beam. As a result the focus features a double line with a *zero* if the incoming light is polarized perpendicular to the line (top). For the parallel case and with a single lens, due to remaining z-polarized light components, the *zero* contains light components. In 4PI optics, these components interfere to zero in the focal plane.

3.3. Potential line-shaped point spread function with a single beam

As mentioned in section 2.4, a semi-circle phase plate can generate a *zero*, that is enclosed by the field in one lateral direction, if illuminated by light that is polarized linearly in the direction parallel to the phase step at the phase plate, as shown in Fig. 3.4 (top). For light polarized perpendicularly (c.f. Fig. 3.4, bottom), the center is filled with z-polarized light components. Therefore this arrangement is inadequate for single objective lens STED.

For 4Pi, on the other hand, this arrangement features a *zero*, enclosed by the field in y and z-direction (cf. Fig.3.5). The on-axis z-polarized components of the counterpropagating beams cancel out in the focus but persist below and above the focus. Thus, they give rise to axial resolution enhancement if used as a STED pattern.

This *zero* is generated, because the z-polarized components in the center are phase-shifted by π against the x and y-polarized components in the outer regions. For constructive interference of the outer regions, the interference in the center is, correspondingly, destructive. Z-polarized components that fill up the center in the single objective lens case, are encountered above and below the focal plane in the 4Pi optics case.

This way a *zero* for two dimensional resolution enhancement can be generated with a single beam. The corresponding PSFs for the excitation are shown in Fig. A.1. This approach seems to be a simple and favourable illumination pattern for two dimensional superresolution microscopy with a single beam. However, if dipole characteristics of the fluorescent probes are considered, drawbacks of this approach arise. The non-uniformly polarized beam will not suppress fluorescence of fixed dipole emitters that are not in line with the polarization [66]. Therefore, STED efficiency decreases and in consequence the resolution is compromised. Calculating the remaining fluorescence for a 765 nm 80 MHz, STED laser of 230 mW for a line length of 2.1 μm and excitation at 635 nm results in a resolution of 95 nm in z-direction and 26 nm in y-direction (cf., Fig. 3.4).[1]

Another drawback of this approach is, that power can not be adjusted individually in order to adapt resolution in y- and z-dimension. However, these drawbacks can be overcome with an alternative approach at the cost of slightly more complexity. This approach requires the combination of two beams for a two dimensional illumination pattern. Here, laser power can be balanced between the two beams. To avoid loss of efficiency when considering dipole dependency, and to achieve similar resolution in the xz- and yz-plane, an approach employing circular polarization was considered.

---

[1] Additionally, if the dipole emitters have fixed axes, they will be imaged elliptically, to some – orientation dependent – extent [67].

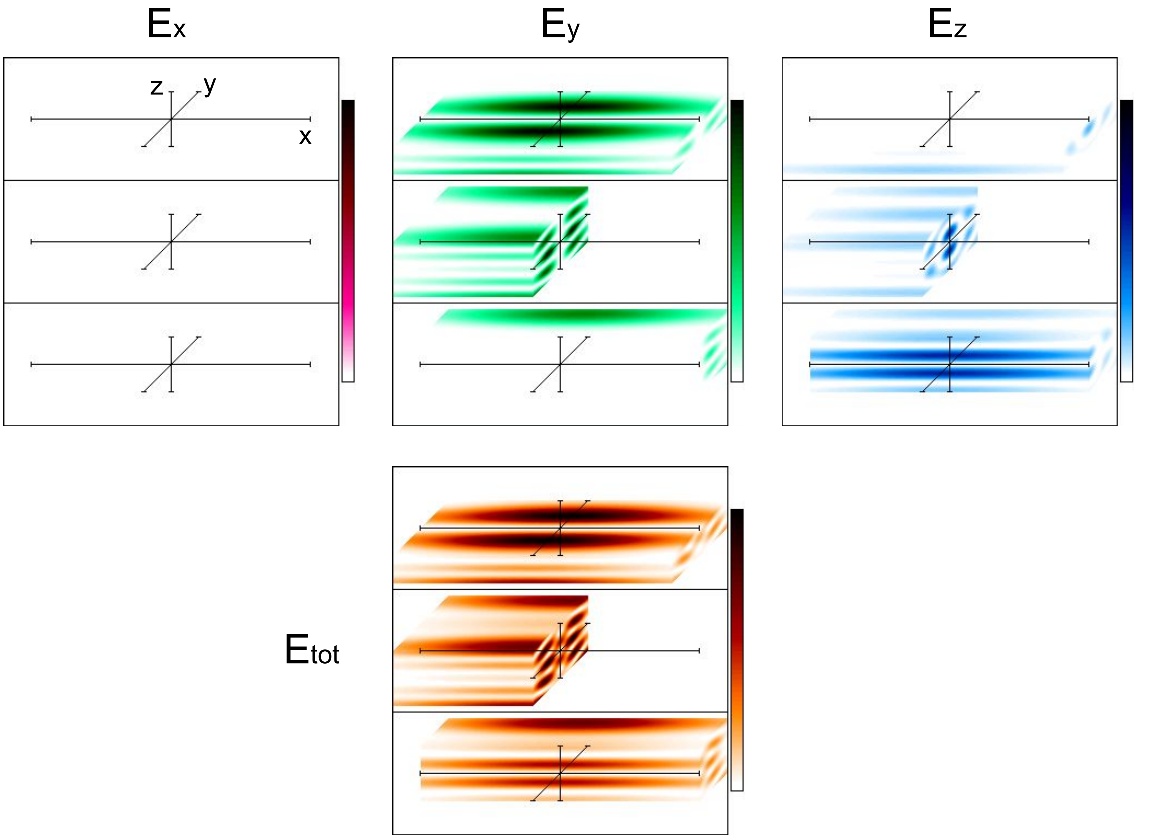

Figure 3.5: STED PSF with a single STED beam and linear polarization. The upper row shows the contribution of the three directions of polarization: Polarization in x-direction (magenta, here negligible), in y-direction (green), and in z-direction (blue). The sum of all components, E_{tot}, is shown in red. For each set, central cuts in xy-plane (top), in yz-plane and in xz-plane (bottom) are shown in 3D-view with a aspect angles of 45° each. The axis scaling is 1 µm x 1 µm x 5 µm. Since linear polarized light is used, y-polarization components prevail. In z-direction, only z-polarized components occur. Components polarized in x-direction are four to five orders of magnitude smaller and since the color scale is linear they are represented as zero. Molecules with a dipole essentially oriented in x- direction will be less efficiently depleted.

3.4. Approach combining two STED beams

To allow the use of circular polarized light, the illumination pattern has to be composed of two distinct beams that overlay incoherently (with respect to each other) in the focus. In this approach, the depletion PSF is a combination of a PSF featuring a *zero* in lateral dimension and another one featuring a *zero* in axial direction. A similar combination was already used in a single spot 4Pi-STED with a constructively interfering PSF of a vortex plate and a destructively interfering PSF.

The illumination patterns in the cavity need to be phase shifted against each other by $\lambda/2$. This can be achieved using a $\lambda/2$ wave plate with its fast axis orthogonal to the polarization axis of one linear polarized STED beam inside one arm of the cavity. In this configuration, two beams that are polarized perpendicular to each other have a phase shift of π.

Implementing a $\lambda/2$ plate in one of the cavity arms needs to be compensated for by a glass block of the same refractive index in the second arm to avoid a wavelength-dependent path length and thus phase shift.

Therefore, it is favourable to use two $\lambda/4$ plates instead of shifting each path by $\lambda/4$ that adds to a total shift of $\lambda/2$. For circular polarization another set of $\lambda/4$ plates is introduced at an angle of $45°$ relative to the polarization plane. The resulting PSF is shown in Fig. 3.6. Calculations, in this case, predict a resolution of 36 nm in lateral and in axial direction with the same laser intensities as for a single-beam approach. Again, fixed, random orientated dipole emitters are considered (cf., Table A.2). Although the setup is slightly more complex and alignment becomes more elaborate due to an additional laser beam, it should be considered because of the potential improvement in resolution.

The resolution is power limited. For a longer line, the fluorescence is depleted less efficient when laser power cannot be increased. Fig. 3.7 shows the predicted resolution for 230 mW STED power with a 80 MHz pulsed titanium sapphire laser at 765 nm and with excitation at 635 nm for different lengths of the line focus.

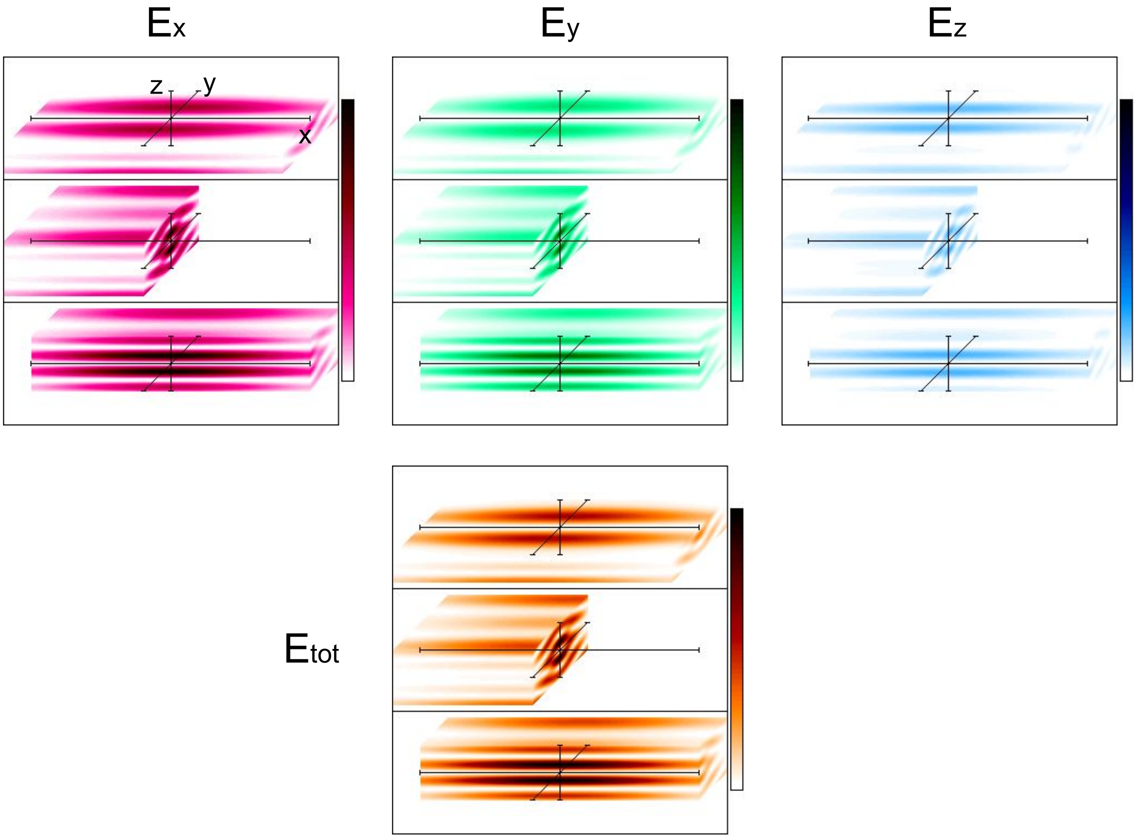

Figure 3.6: STED PSF as a sum of two STED beams. Since circular polarized light is used, all three polarization components are represented almost equally in all three dimensions. The 3D views and color codes are the same as in Fig. 3.5. All molecules are efficiently depleted, irrespective of their dipole orientation.

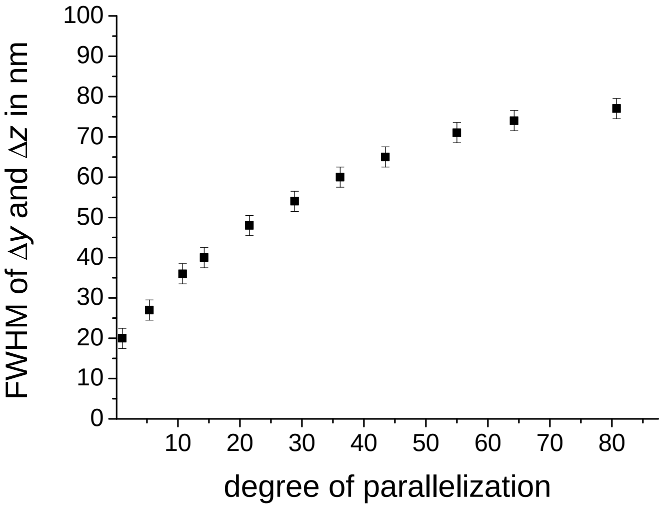

Figure 3.7: Resolution scaling in dependence of the degree of parallelization for the two-beam approach. Laser power for the two beams was balanced to achieve comparable resolution for y- and z-direction. The resolution in x remains 240 nm. Power balances for the two STED beams and parameters used for the calculation are shown in Appendix A.2.

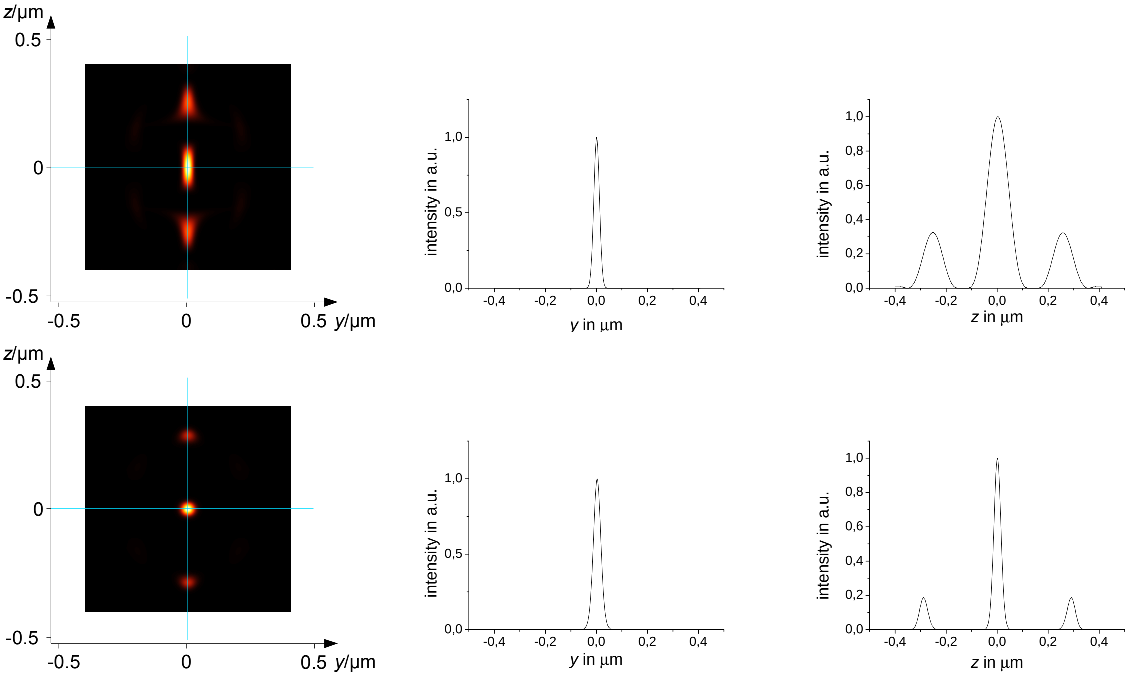

Figure 3.8: Comparison of the effective PSFs for the two different approaches considering random oriented, fixed dipole emitters. In the case of linear polarized light (left), the FWHM in z-dimension is 95 nm, whereas the FWHM for the case of depletion with circular polarized light the FWHM in z- and y-dimension is 36 nm.

4

Optical Implementation

Here, the 4Pi augmented STED setup is described. The beam path and the control parameters are depicted. In addition, the electromechanical characteristics of the 4Pi cavity and of the objective lens support are presented. Since the alignment of a 4Pi setup is a complex task, relevant aspects are discussed in greater detail. The critical alignment parameters are listed and alignment methods are presented.

4.1. Optical layout

The complete optical setup is a combination of a parallelized STED and a novel 4Pi arrangement as shown in Fig. 4.1[1] It consists of the STED and excitation laser sources, a detection unit, the 4Pi cavity with the scanner, and a unit for diagnostics and wide-field detection. The STED laser is a pulsed titanium sapphire laser (Chameleon, Coherent, Santa Clara, USA) with 80 MHz pulse repetition rate. 80 fs pulses are pre-stretched to 2.5 ps in a block out of dense flint (optics workshop, MPIbpc, Göttingen, Germany) of 39 cm length. This step is necessary to avoid nonlinear effects inside the optical fibre. Pulses are stretched to a width of 100 ps by dispersion in an optical fibre (OZ optics, Carp, Canada) of 151 m length. Picosecond pulses or longer are needed to avoid two-photon excitation in the sample. The wavelength has been set to 765 nm. The spectral width behind the optical fibre is 16 nm. A picosecond pulsed diode laser (Picoquant, Berlin) of 635 nm and

---

[1] Here, all focal length of the achromatic (AC) and the cylindrical lenses (CL) are specified.

80 MHz was used for excitation. Timing was accomplished with delay electronics (custom made, MPIbpc, Göttingen, Germany).

The STED beam and the excitation beam are focused into a line via a cylindrical lens, (CL), (Qioptiq, Feldkirchen, Germany). The STED beam is separated into its two polarization components with the help of two polarizing beamsplitters. Power balance of the two polarization components can be adjusted with a $\lambda/2$-plate in front of the optical fibre output. A Glan-Thomson-Prism (Thorlabs, Newton, USA) cleans the beam from parasitic polarization components to ensure linear polarization. The horizontal polarization component passes a semi-circle phase plate (manufactured by vapor deposition of 1330 nm cryolite at optics workshop, MPIbpc, Göttingen, Germany) as depicted in Fig. 2.8. The phase shift of π for one side of the laser line leads to a focus that features a double line with a *zero* in its center, as described in section 3.3.

The semi-circle phase plate is placed in the focal plane of the cylindrical lens. This plane is imaged into the back focal plane of the scan lens (Leica microsystems, Mannheim, Germany) on the galvanometric mirror (Cambridge Technologies, Lexington, USA) with the help of two achromatic lenses. The two STED beams are merged at a second polarizing beamsplitter. However, these two components overlay incoherently[2]. For the excitation beam only the horizontal polarization component is needed. The three beams are merged at a dichroic mirror (F37-736, AHF, Analysentechnik, Tübingen, Germany) before entering the scanner and the 4Pi cavity. The back focal plane of the scan lens is imaged into the back focal plane of the objective lenses with the scan lens and the tube lens (Leica microsystems, Mannheim, Germany). At the entry to the 4Pi cavity the beams are split with a 50% non-polarizing beamsplitter (Newport, Irvine, USA). Objective lenses of magnification 100 and NA 1.44 with correction collars are used (Leica microsystems, Mannheim, Germany). The $\lambda/4$-plates inside the cavity (B. Halle Nachfolger, Berlin, Germany) are orientated as depicted in Fig. 4.1. They are fixed with a custom made mount out of brass, that is fixed to the breadboard (not shown).

Fluorescence light leaving the cavity is chromatically separated at a custom made dichroic mirror (F73-746, AHF, Analysentechnik, Tübingen, Germany) before entering the detection path. Here, it is further cleansed of remaining light components

---

[2] Incoherence is assured by slightly different path-lengths and perpendicular polarization

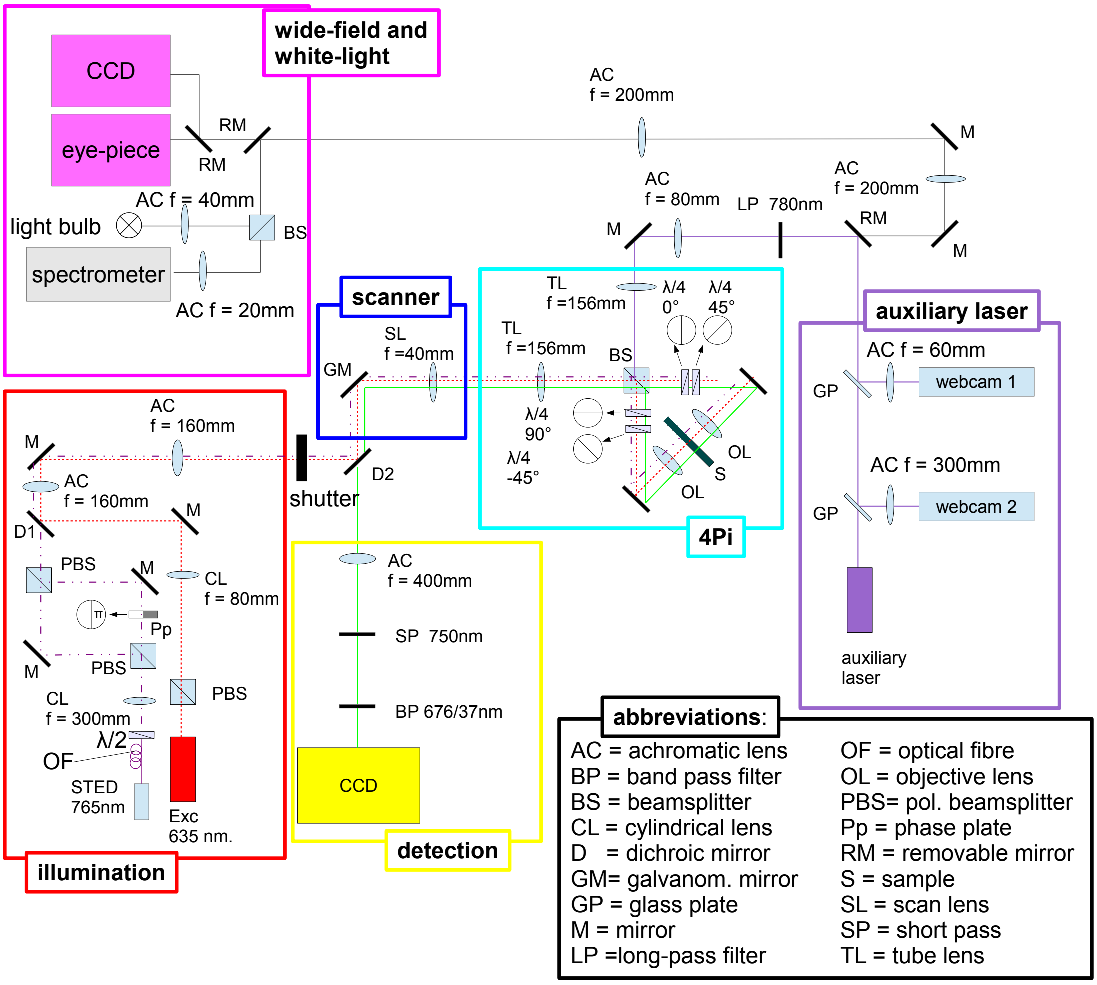

Figure 4.1: Diagram of the optical pathway. The STED beam and the excitation beam are focused into a line with a cylindrical lens and divided into its two polarization components via a polarizing beamsplitter (PBS). One polarisation component passes through a semi-circle phase plate. The excitation beam is shaped into a line via a cylindrical lens and merged with the STED beam via a dichroic mirror. Two lenses image the foci of the cylindrical lenses of the STED and excitation beam onto the back focal plane of the scan lens (SL). A galvanometric tilt mirror is placed in this plane for scanning the line focus in one dimension. Light then passes the tube lens and enters the cavity through a non-polarizing 50% beamsplitter. Each cavity arm has two achromatic $\lambda/4$ wave plates in 0° and 45° orientation for one cavity arm and in 90° and -45° orientation in the second cavity arm. Light leaving the cavity is descanned and fluorescent light is filtered at the dichroic mirror (DM) and a bandpass filter (BPF), and focused onto an EMCCD camera.

of excitation and STED light by a bandpass filter (F37-677, AHF Analysentechnik, Tübingen, Germany) and a shortpass filter (FF01-750/SP-25, Semrock, Rochester, USA). An EMCCD (iXon 897, Andor Technology, Connecticut, USA) detects the remaining fluorescence signal.

A second light path is used for diagnostics and wide field detection. STED and excitation light is blocked at a long pass filter (FF01-776/LP-25, Semrock). An adjustment laser with a wavelength of 787 nm is coupled into the cavity. The focus of this auxiliary laser is imaged by a webcam (Philips, Amsterdam, Netherlands). A second webcam images the back focal plane of the system. A removable mirror allows to swap between the auxiliary laser path and the white light illumination and widefield path. It contains an eyepiece (Leica Microsystems, Mannheim, Germany) and an additional CCD (PCO, Melbourne, Australia) as well as a light bulb and a spectrometer (Avantes, Broomfield, USA) for cavity dispersion adjustment with the help of white light.

4.2. 4Pi cavity design

The 4Pi cavity design implemented here is a further development of a 4Pi setup presented in [34], [68] and [29]. The main objective of the redesign has been to stabilize the setup against mechanical vibrations and to minimize thermal drift to guarantee stable optical conditions over many minutes. In this respect, units that are prone to vibrations have been replaced. For low thermal drift materials with similar thermal properties have been selected. In particular, the design of the mounting frame for the objective lenses has been reconsidered. In former designs the frame was directly fixed to the stand of an upright confocal microscope (Leica microsystems, Mannheim, Germany). Such a frame is rather flexible. Therefore, it was susceptible to mechanical vibrations, which would affect STED imaging adversely. Rather than attaching a cavity to a commercially available microscope as in previous studies, a support for the two objectives has been designed and constructed that stands independently and directly mounted on the optical table (cf., Fig. 4.2). As added value, it has an extremely rigid design. It is built out of three platforms that are connected by pillars.

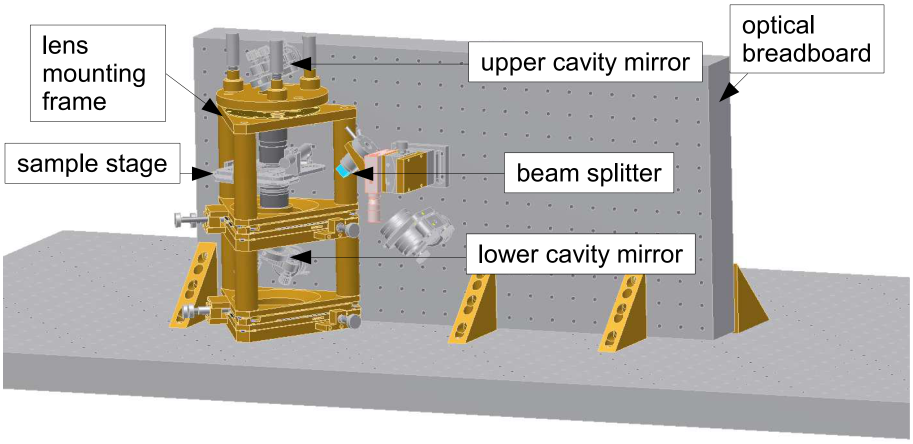

Figure 4.2: CAD drawing of the basic 4Pi setup. The cavity is arranged in a vertical manner. Objective lenses are attached to a support made of brass for similar thermal expansion compared to the objective lens mechanics. The z-stage is mounted directly to the head of the lower objective lens in order to minimize susceptibility to drift. Cavity mirrors and tube lens are attached to an optical breadboard that is mounted on an optical table.

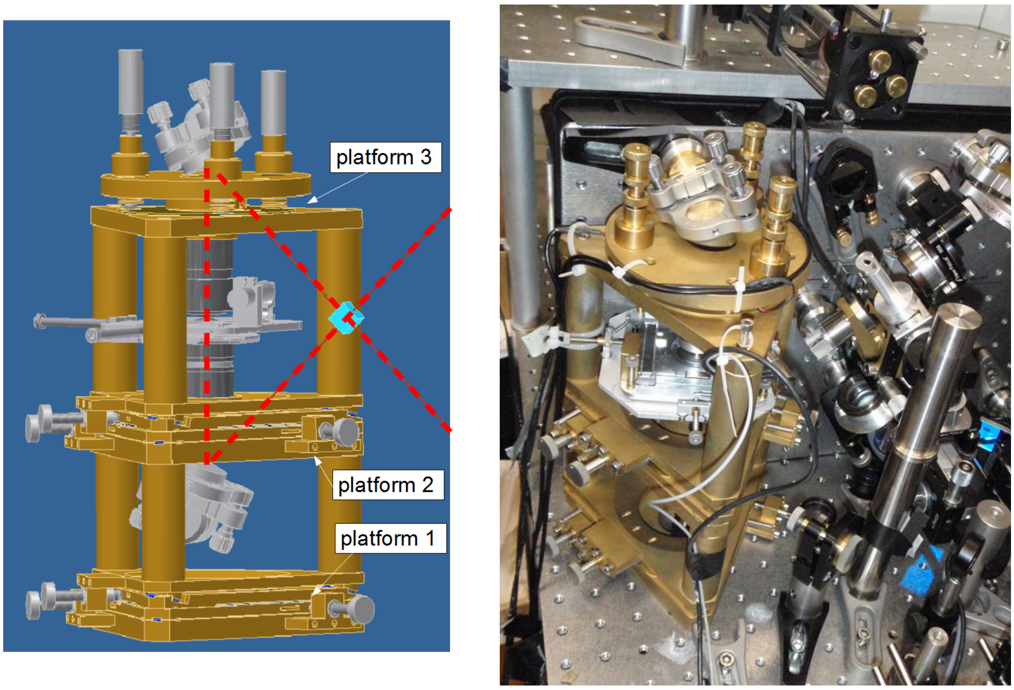

Figure 4.3: CAD drawing (left) and photo (right) of the 4Pi cavity and the objective lens support. The cavity is arranged in a vertical manner and the optical path is shown in red. The support consists of three platforms. Platform 1 allows lateral adjustment of the entire support via fine adjustment screws on each side. An additional screw allows to change the distance between platform 1 and 2, which defines the length of the lower pathway. Platform 1 and 2 function as adjustment tool for the upper objective lens. The three adjustment screws of platform 2 allow lateral and axial movement of the whole upper section of the support against the lower one. The upper objective lens can be tilted with the help of the upper platform. It is attached to a bending brass sheet that serves as a joint. The pressure of the piezoelectric actuators on the surface defines the tilt of the objective lens towards the rest of the lower part of the support.

For thermal reasons brass, that is also used in objective lenses mechanics, has been chosen as material instead of aluminum, as in previous studies. While aluminum has a CTE of $23.1 \cdot 10^{-6}$ K^{-1}, brass has a value of $18.4 \cdot 10^{-6}$ K^{-1}[69]. This has in the past caused non-uniform thermal expansion.

For easy sample handling a 4Pi arrangement with a vertical cavity has been chosen in contrast to the horizontal type arrangements chosen by [42] and [30]. Fig. 4.2 shows a CAD (Autodesk Inventor 2009, San Rafael, USA) drawing of the optical layout. The setup can be divided into two subunits, the lens mounting frame and the cavity unit. The cavity unit, consisting of two cavity mirrors and a beamsplitter, is attached to an optical breadboard (Newport, Newton, USA) that is fixed on top of the optical table. It should be noted that there is no direct mechanical contact between the mirrors and the objective lens mounting frame. This helps to prevent the transmission of any mechanical vibration of the vertical breadboard to the objective lenses or to the sample stage. The lens mounting frame is inserted into the cavity and can be removed, e.g. for pre-alignment. This architecture largely decouples the objective lens alignment from the cavity alignment.

The beamsplitter can be adjusted by rotating around one axis with a goniometer (Newport, Newton, USA) with fine adjustment screws and around the other axis by a fine adjustable rotating lens mount (Qioptics, Feldkirchen, Germany). The cavity length can be adjusted by moving the beamsplitter vertically on its linear stage (Newport, Newton, USA) . The beamsplitter support, the mechanics of the platforms and the objective lens mounting frame are shown in detail in Figs. 4.3, 4.4 and, 4.5, respectively.

The cavity mounting frame (cf., Fig.4.3) allows for lateral and axial adjustment of the objective lenses within the cavity unit. It consists of three platforms that can be moved against each other. Platform 1 allows lateral shift of the entire support. It is used to center the objective lenses in the beam path. The axial position of the objective lenses, and thus the length of the two cavity arms, can be adjusted. Platform 2 holds the lower objective lens and allows lateral and axial shift of the upper lens relative to the lower lens. Platform 3 holds the upper objective lens, allowing the lens to be tilted and lifted.

The platforms are divided into four single sub-plates (cf., Fig. 4.4). Plate 1 is fixed to the optical table or to the pillars below, respectively. Plate 2 can be moved against plate 1 with fine adjustment screws on each side. At the contact areas sapphire windows have been inserted to provide minimal friction. Plate 3 includes a wedge and can be moved with the help of the upper adjustment screw. This way the height of the platform can be adjusted. Plate 2 and 4 are connected by a bending sheet, that prevents lateral shift and gives a prestressing, that pulls the plates together when the adjustment screw is loosened. Mechanically, platform 1 and platform 2 are more or less identical. The only difference is found in the design of plate 1; the thread for the objective lens in platform 2 is absent in platform 1.

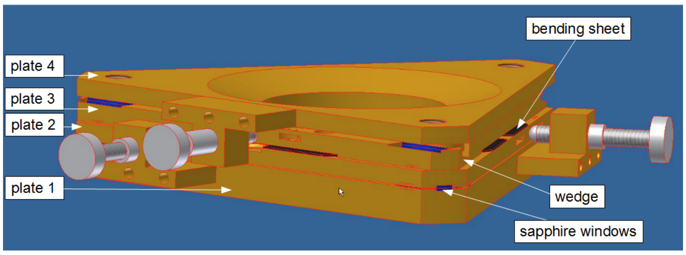

Figure 4.4: CAD drawing of the platform 1. It consists of four plates that can be moved against each other. Plate 2 enables lateral shift if moved against plate 1 with the help of fine adjustment screws. The wedge of plate 3 allows to alter the height of the platform. The bending sheet, that is attached to plate 2 and 4, provides a prestressing and prevents lateral shift, when the platform's height is changed. Sapphire windows at the contact areas minimize friction.

Platform 3, on top of the support, consists of only two plates and holds the upper objective lens. The lower plate is attached to the pillars. A second plate is placed on top with a thread for the objective lens and three piezoelectric actuators (Physik Instrumente, Karlsruhe, Germany). The plates are fixed using a bending sheet in between for flexible movement. This way the upper plate can be tilted and lifted against the lower plate for fine adjustment of the upper objective lens's focus with respect to the lower one. A rough manual adjustment can be done with the adjustment screws located on top, while the fine adjustment is controlled by the piezo drives.

The sample stage is directly attached to the objective lens. This concept was used in [67] and [32] and has proven to show low thermal drift of the object with respect to the focus. A piezo drive enables stage scanning in axial direction.

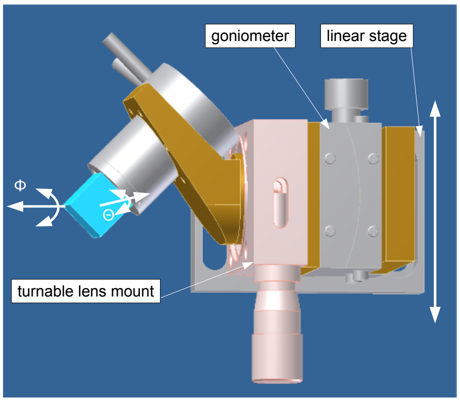

Figure 4.5: CAD drawing of the beamsplitter support. The goniometer allows to change the angle Θ and the lens mount allows to change the angle Φ with the pivot point at the center of the beamsplitter.

The beamsplitter is one of the most important parts and its position determines the length of the two cavity arms as well as the light path for the lower objective lens. It therefore needs to be attached in a robust manner with respect to the cavity mirrors still allowing alignment. As a solution to this requirement, a solid support that consists of a linear stage, a goniometer, and a rotatable lens mount has been constructed (cf., Fig. 4.5). The beamsplitter is bonded to a tripot piezo drive (S316 Physikinstrumente, Karlsruhe, Germany). The piezo actuator is attached to the lens mount with a custom made spacer piece. Finally, the lens mount is attached to the goniometer placed on top of a linear stage. This arrangement enables a rough three axes alignment.

4.3. Instrument control

The entire hardware is controlled with the help of a LabVIEW program. Parameters are converted into analogue signals with the PCI-DAC and fed into a custom made control unit that adapts the signals for the various hardware components, where needed. The control parameters are depicted in Fig. 4.6. Fine adjustment is carried out by moving the piezo drives of the beamsplitter support and the upper objective. The trigger and the signal for the galvanometric mirror and the piezo actuator for the z-scan allow synchronisation of the scanning process and the image acquisition.

The external shutter inhibits illumination of the sample when no imaging process takes place.

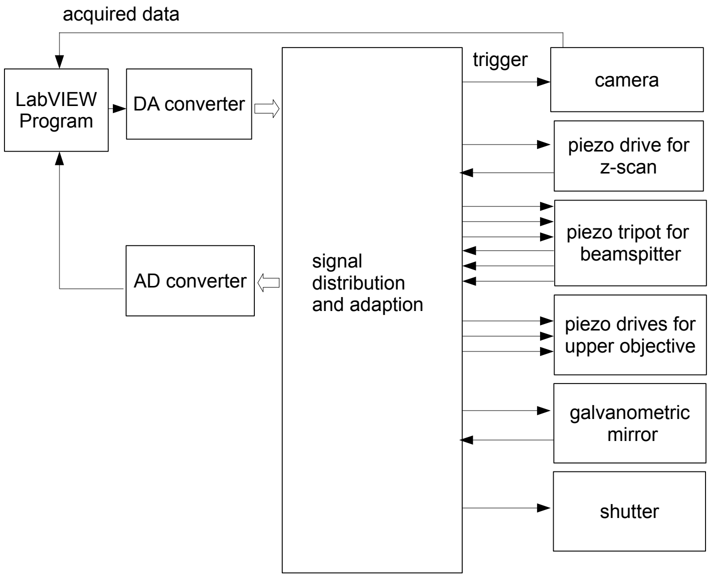

Figure 4.6: Diagram of the control unit. A LabVIEW program (LV 8.5, National Instruments, Austin, USA) has been designed to synchronize the scanning and acquisition process and for the fine adjustment control. The output parameters are fed to a DAC (PC-6014, National Instruments) and translated to analogue outputs. The signal distribution unit adapts and amplifies the DAC outputs by standard operational amplifiers, where necessary and provides voltage supply. The output signals control the various devices. Feedback signals are returned to the control and further to an ADC (PCI-6703, National Instruments) that is read in by the LabVIEW program for further processing.

The scan cycle is shown in Fig. 4.7. After each scan step of the galvanometric mirror a de-scanned line image is taken. Only the illuminated area is read out. The line array is fed into the LabVIEW program building up an image line by line.

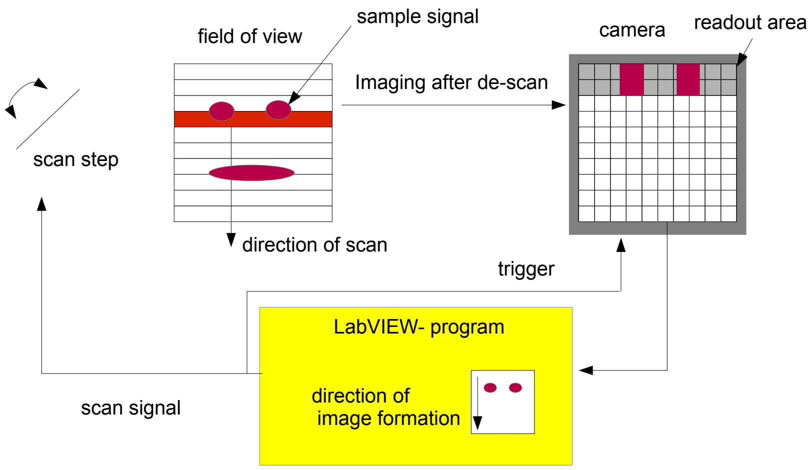

Figure 4.7: Diagram of the scan cycle and image acquisition process. The scan is synchronized with the camera trigger. After each scan step a line image is taken. A line array of pixels is read out after de-scan and fed to the LabVIEW program. This way an image is build up line by line.

4.4. Optical alignment

A number of basic parameters that need to be adjusted in order to successfully image with 4Pi optics are already referred to in [68]. For the particular application in parallel 4Pi and the specific setup used here, some parameters are slightly different and have to be reconsidered.

4.4.1. Lateral beam adjustment

The two opposing objective lenses have to be carefully aligned. As a result of a misalignment the two foci do not overlap completely and interference will be incomplete. Consequently, it is helpful to image the focal plane and the entrance pupil plane of the objective lenses for alignment. To get information about the whole area of the objective lenses' entrance pupil an additional auxiliary laser of 787 nm wavelength, that illuminates the entire entrance pupil, is used. The back focal plane and the focal plane are imaged by two webcams. As described in [68], the focal image as well as the interference pattern in the back focal plane help to inspect whether the foci of the two objective lenses overlay. In a standard 4Pi setup, the interference of the transmitted light in a Sagnac type interferometer is maximal for light returning to the incoming path, as described in section 2.2. Thus in the presented setup, the inserted waveplates invert the interference pattern. Transmitted light gets an additional phase shift of π as it passes the cavity in one direction and no additional phase shift in the opposite direction. This means that the constructive and destructive arm are swapped in comparison to the standard Sagnac type cavity. Table A.2 shows the effect of the waveplates on the counter-propagating beams.

4.4.2. Angle matching

The two beams in the cavity arms should not only overlay in the focus, but should also enclose an angle of 180°. A mirror sample can be used to analyse this parameters. The resulting interference pattern in the image plane and in the back focal plane of the two reflexes should feature constant phase over the whole image area. In case of a tilt, the interference pattern in the image plane features stripes or decentered rings. Fig. 4.8 shows the resulting images for aligned and misaligned

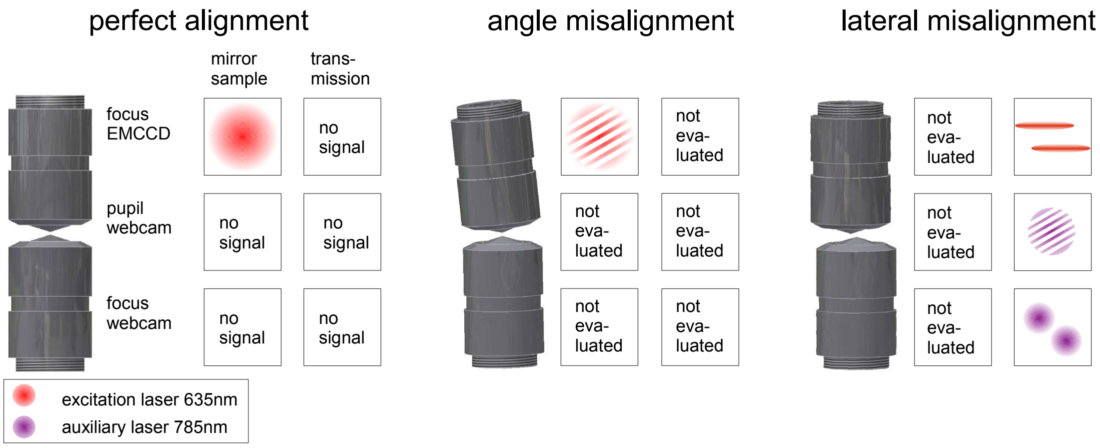

Figure 4.8: Objective lens adjustment. The image series shows possible misalignments of the objective lenses. Next to the sketch of the objective lenses (extreme cases are shown) the relevant scanned image on the EMCCD and the webcam images are shown (left). The image on the left shows the resulting feedback signals for perfect alignment of the two objective lenses. The image of a mirror sample on the EMCCD should show constant intensity. For transmission light, the back focal plane should show destructive interference as well as the focus of the auxiliary laser. In transmission mode the beams interfere destructively and all images should feature minimal intensity (middle). If the angle of the two objective lenses is misaligned, the mirror sample shows inference fringes on the EMCCD and the interference pattern of the auxiliary laser is shifted (right). If the objective lenses are shifted against each other, the image of the back focal plane shows interference fringes and the foci are misplaced.

angles. It should be noted, that a tilt of one objective lens shifts its focus laterally. Therefore the lateral beam adjustment and the angle matching need to be repeated iteratively until optimal alignment is achieved.

4.4.3. Adjusting the sample

The sample should be placed horizontally, in order to minimize aberration. Also, there should not be any air bubble in the immersion giving rise to aberration. For this alignment the webcam images of the adjustment beam can be evaluated. The image of the pupil shows a black spot if there is an air bubble in the immersion. In this case, the sample has to be removed and inserted back carefully and slowly to avoid air bubble enclosure. A perfect interference pattern exhibits straight lines. If there are s-shaped curves at the outer regions of the pupil, the sample might be tilted and should be put in a more horizontal position to avoid astigmatism. The shape of the interference stripes can also give information about spherical aberration that occur if the correction collars of the objective lenses are not set properly or refractive index mismatch of the immersion or the sample is too thick.

4.4.4. Color dispersion

The two cavity arms must have equal length with a difference smaller than the coherence length of the light to ensure interference. However, the optical pathway is wavelength dependent because of residual mismatch of the optical elements and their dispersion. The optical pathways for the excitation and STED wavelengths should not differ. The color dispersion can be aligned using a white light source. A light bulb of a torch is used for a broad white light spectrum. All parameters stated above have to be aligned adequately in order to allow interference of the white light, that has a short coherence length. Again, a mirror sample has been used for alignment. If the alignment is adequate, colored newton rings appear in the pupil image (cf., Fig. 4.9). The image is focused to a fibre spectroscope that shows maxima for constructively interfering wavelengths and minima for destructively interfering wavelength (cf. Fig. 4.10). A fine adjustment screw at the bottom of the pillar construction can be used to adjust the length of the cavity arms. If the range of this shift is not sufficient, the position of the beamsplitter cube in the cavity needs to be changed and consequently the path length in the dispersive glass. This way, constant phase difference for a broad range of wavelengths can be provided.

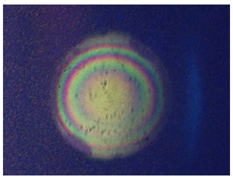

Figure 4.9: Back focal plane webcam image for white light. Coloured rings indicate correct dispersion alignment.

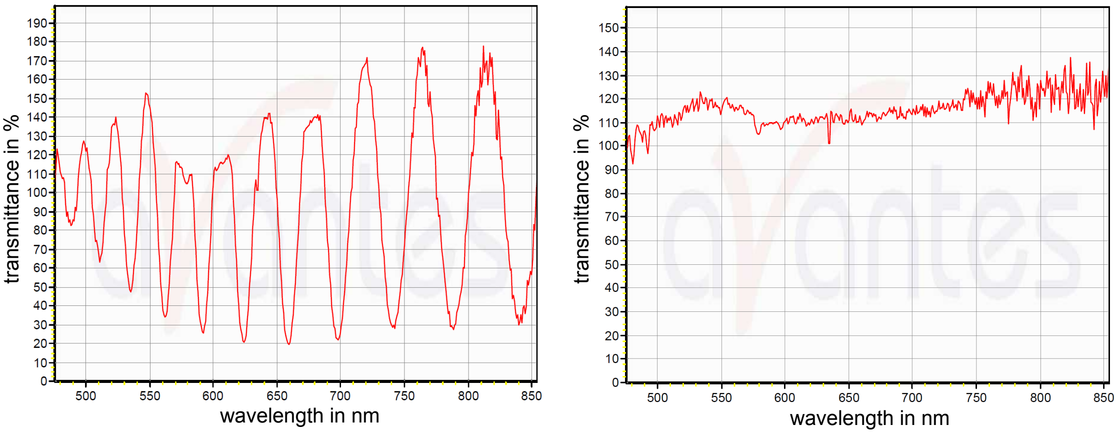

Figure 4.10: Spectrum for an interfering white light source with mismatching color dispersion (left) and matching color dispersion (right). A modulation in transmittance (right) with respect to λ indicates that the cavity length is wavelength dependent and light interferes constructively or destructively, respectively. If the alignment is optimal (right), the transmittance is constant for a wide spectral range.

4.4.5. Lateral color error

When the tube lens and the objective lens are not well aligned, but are inclined against each other, a color dependent lateral shift, here referred to as lateral color error, will be introduced. Imaging the back scattered light of a gold bead sample allows to analyse this error. The alignment procedure should start with the upper objective lens. If the image of gold beads appear laterally shifted for different wavelengths, the tube lens has to be tilted such that the images for the two colors overlap. After the color error is adjusted for the upper objective lens, the lower objective lens is adjusted. Since tilting the tube lens would now misalign the color error for the upper objective lens again, adjustment has to be done with the help of the beamsplitter. The introduced error for the angle matching has to be compensated for with the help of the lower cavity mirror. If needed, adjustment has to be iterated.

4.4.6. STED beam and phase plate alignment

The quality and alignment of the STED beam are of particular importance for the performance of the microscope. Misalignment and aberration may lead to imperfect *zeros* and loss of peak intensity of the STED PSF. In Figs. 4.11 and 4.12, the effects are shown in comparison to the perfectly aligned no-aberration case.

If the beam is not centered in the back aperture or the phase plate is not centered in the pupil the quality of the *zero* is affected. Strong spherical aberration and astigmatism ($\lambda/2$) lead to loss of peak intensity, the *zero*, however is preserved. These effects are similar to effects in single-lens setups, as described, e.g., in [70].

Spherical aberrations were minimized with the help of the objective lenses' correction collars. The procedure is described in detail in [68].

perfect alignment and no aberrations:

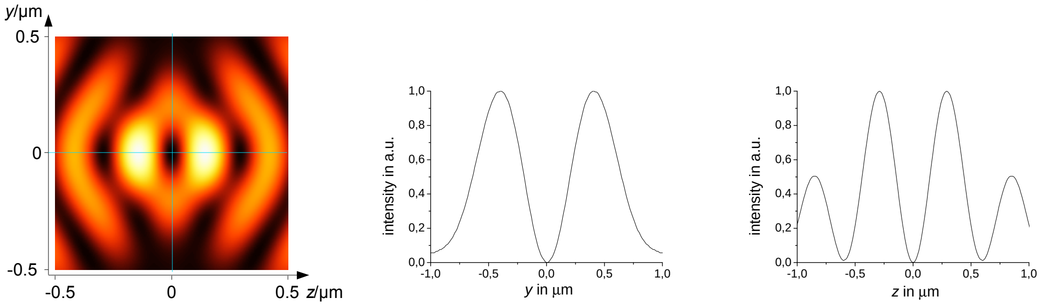

beam not centered in back aperture (1 mm misplacement):

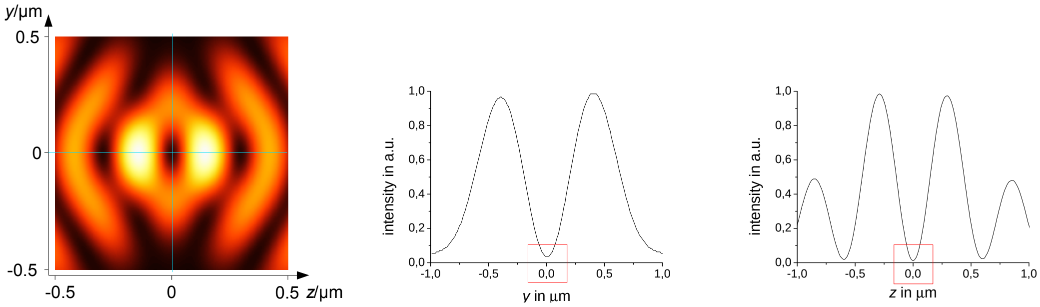

phase plate not centered (0.5 mm misplacement):

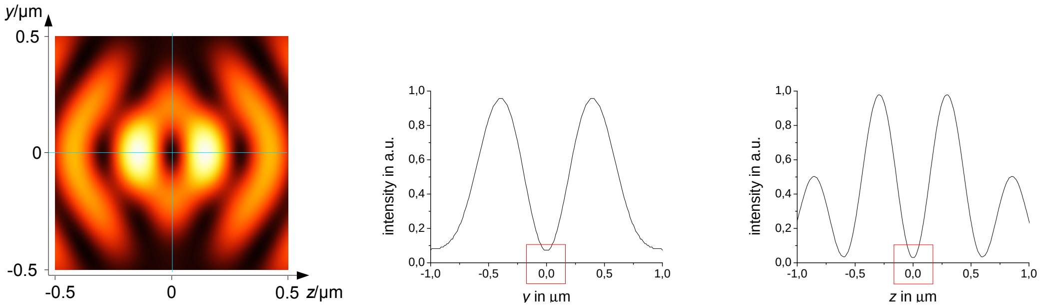

Figure 4.11: Effect of misalignment on the STED PSF. A cross section in yz-direction of the resulting PSF (left column) and the profile along y- and z-axis in the focus (right) are shown. These misalignments lead to imperfection of the *zero* and thus loss of signal that may lead to loss of resolution performance.

perfect alignment and no aberrations:

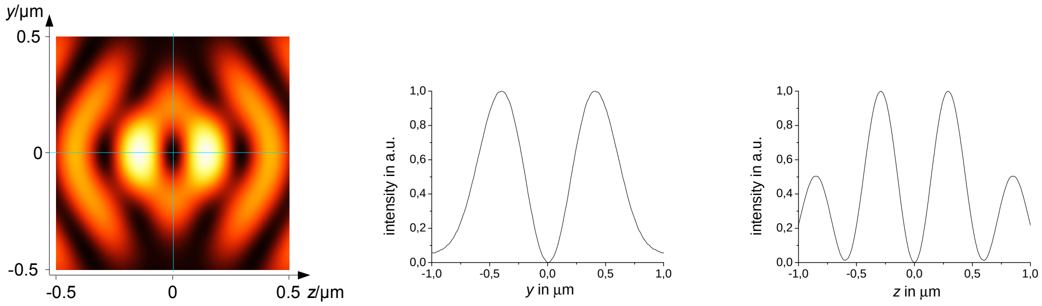

spherical aberrations ($\lambda/2$):

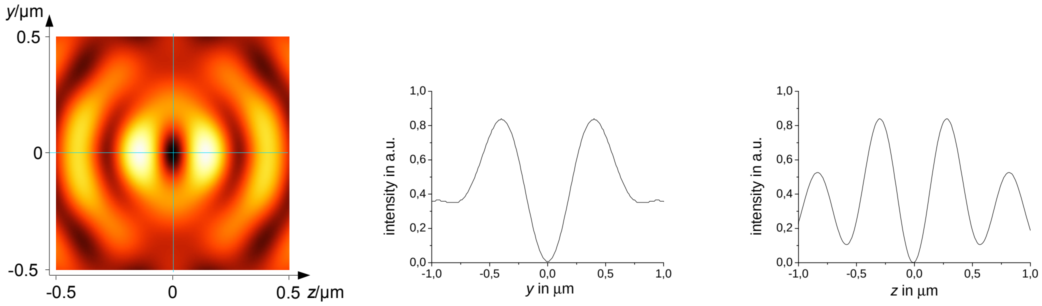

astigmatism ($\lambda/2$):

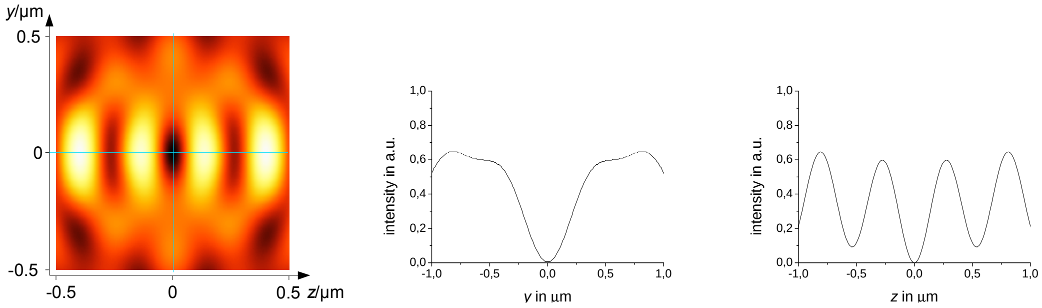

Figure 4.12: Influence of aberration on the STED PSF. A cross section in yz-direction of the resulting PSF (left column) and the profile along y- and z-axis in the focus (right) are shown. These errors do not affect the *zero*, but the loss of peak intensity may lead to loss of resolution performance.

5

Experimental Results

In this chapter, the performance of the developed setup is characterized. With this objective, a number of technical samples have been imaged. The first section deals with measurements of qualitative analysis of the PSF and the second section with the resolution enhancement achieved to present.

5.1. Imaging of the PSFs

Since residual misalignment and aberrations hamper the performance of the microscope, a number of analytical measurements have been carried out. To get an impression of the PSF of the system a number of technical samples have been imaged.

To get a first impression about the quality of the adjustment, a z-stack of wide field images of a mirror sample have been taken with the STED laser. The residual intensity components that pass the dichroic mirror (approximately 0.1% of the total intensity) have been imaged after removing the bandpass filters in the detection path.

The sample preparation methods are listened in appendix A.4. A stack of wide-field images has been taken while scanning in z-direction. A central cut of the image in the yz-plane is shown left hand in Fig. 5.1. The measured image is very similar to the theoretical prediction. It should be noted that the z-polarized components do not show up in the image, because a reflection is imaged and not the PSF as such. The result is in accordance with the calculated image (cf., Fig. 5.1, right).

An mirror reflection is a good rough estimate of the PSF, especially concerning misalignment of the beam in the back focal plane and aberrations. However, errors such as lateral color error and estimation of the *zero's* quality are analyzed with the help of a scattering point object.

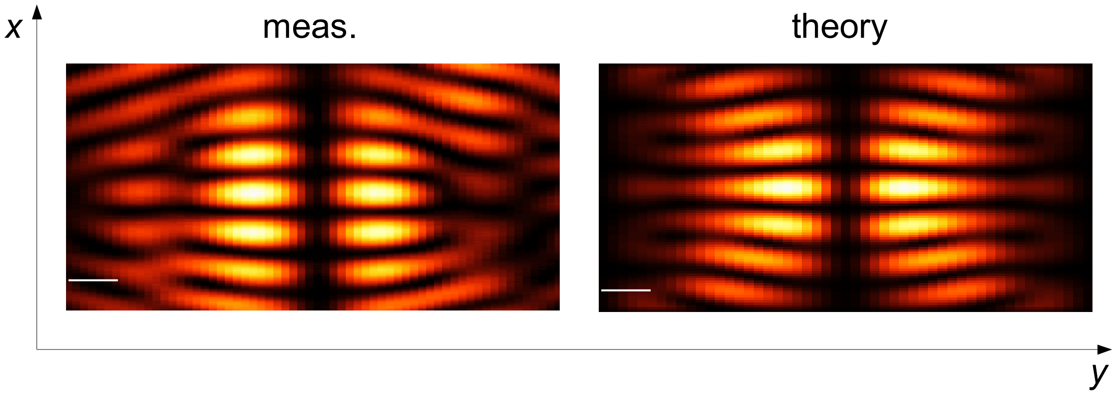

Figure 5.1: Image of a silver mirror sample taken with the STED beam in 4Pi mode. A yz-cut of a z-stack of wide-field images at x=0 is shown. The z-polarized components will not show up in this configuration. Measurement (left) and calculated image (right) are shown. Image size is 2 µm × 1 µm. Scale bar length is 200 nm.

Gold colloids of the size of 40 nm have been used as additional analytical sample. Remaining scattered light is detected through the dichroic mirror, as well. However, since the wavelength between incident and detected light is not shifted, transmitted light cannot be filtered out and will outshine the scattered light. Therefore only the backscattered light of a single objective lens can be observed, while blocking the second cavity arm. The resulting image and the predicted result are shown in Fig. 5.1. The *zero* of the STED beam is positioned at a gold colloid. However, the z-polarized components on axis are imaged ring shaped on the camera, as theoretically predicted. The result gives useful information about correct placement of the phase plate, beam shift in the back focal plane, and lateral color error. To test the performance in 4Pi mode, images of fluorescent microsphere samples have been taken. Fig. 5.3 shows an image of a fluorescent microsphere taken with the excitation laser. Unfortunately, no technical sample was available to image the PSF of the STED beam likewise because of its near infrared wavelength. These result demonstrates that the setup enables 4Pi measurements with a line-parallelized scan.

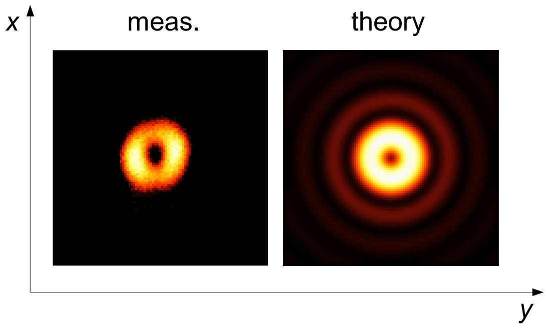

Figure 5.2: Image of a gold colloid sample imaged with the lower objective lens. Image size is 2 µm × 2 µm. Measurement (left) and calculated image (right) are shown.

5.2. Resolution enhancement

Several images of fluorescent microspheres in STED mode have been taken. They provide information about the resolving power of the setup. The results show, that superresolution of below 50 nm is possible in two dimensions. Resolution x (along the line) is not enhanced, and yet about 240 nm. Intensity profiles show that 20 nm fluorescent microspheres are partly imaged with a FWHM of only 45 to 50 nm in y-direction and, simultaneously, with a FWHM of 41 nm in z-direction. It has not yet been possible to take a xyz-stack, due to photobleaching of the microspheres. Still the images show the potential for superresolution of the setup. Signal-to-noise ratio is roughly 6 for the xz-image and 13 for the xy-image, evaluated in the region, in which the profiles has been drawn. This SNR is comparable to images taken with a multi-foci STED[71]. However exposure times have been in the order of 10 times shorter at comparable laser dose. A characterization of the EMCCD performance (cf. appendix A.5), showed that hardware binning introduces excess noise due to hot pixels in a typical background image (cf. appendix A.5).

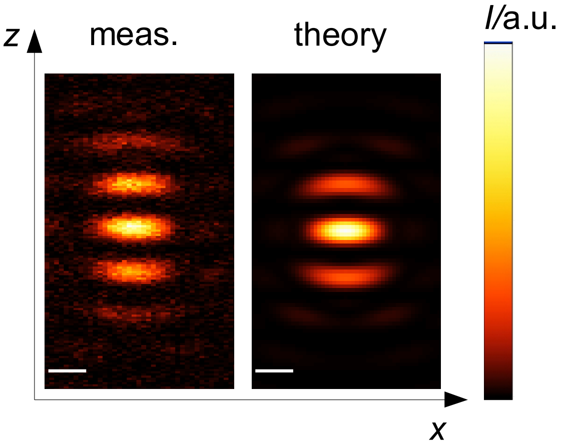

Figure 5.3: 4Pi image of a fluorescent microsphere sample. The fluorescent image taken on the setup (left) is shown in comparison to the calculated field distribution. Image size is 1 µm × 1.7 µm. The scale bar is 200 nm. Exposition time has been set to 10 ms and excitation power 30 µW.

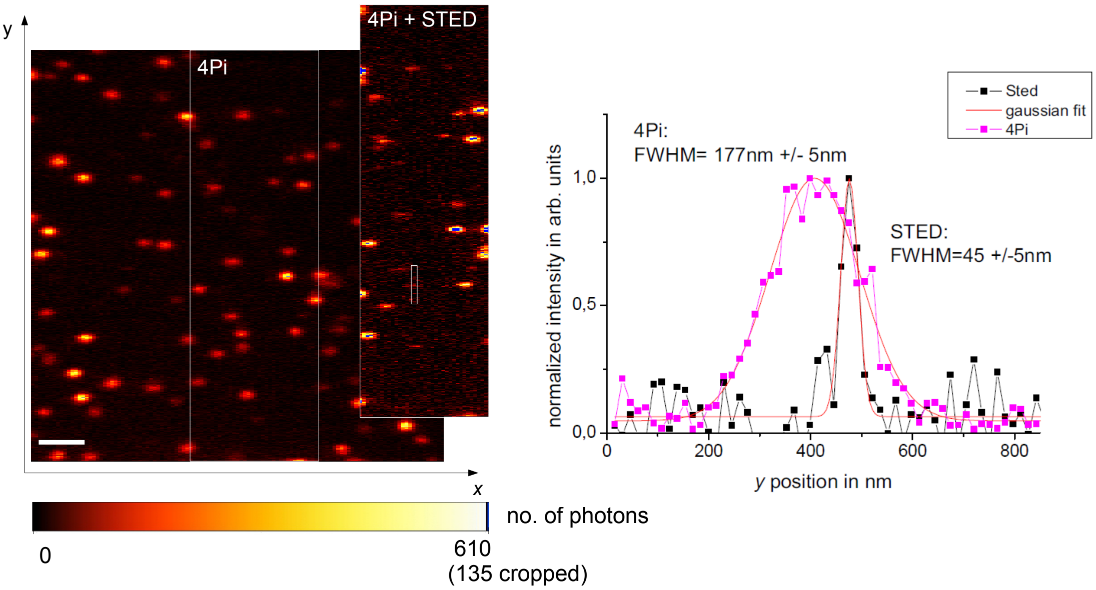

Figure 5.4: xy 4Pi image and 4Pi-STED image of a fluorescent microsphere sample. Image size is 9.6µm × 9.6µm. Due to the line illumination the predicted resolution for 4Pi is 160 nm in x-direction and 240 nm in y-direction. Therefore the microspheres appear elongated. The area indicated by the white frame has been imaged with STED laser switched on directly afterwards. The cropped part shows this area and the resolution enhancement in y-direction. The resulting FWHMs in y-direction are 177 nm for 4Pi and 45 nm for 4Pi STED.

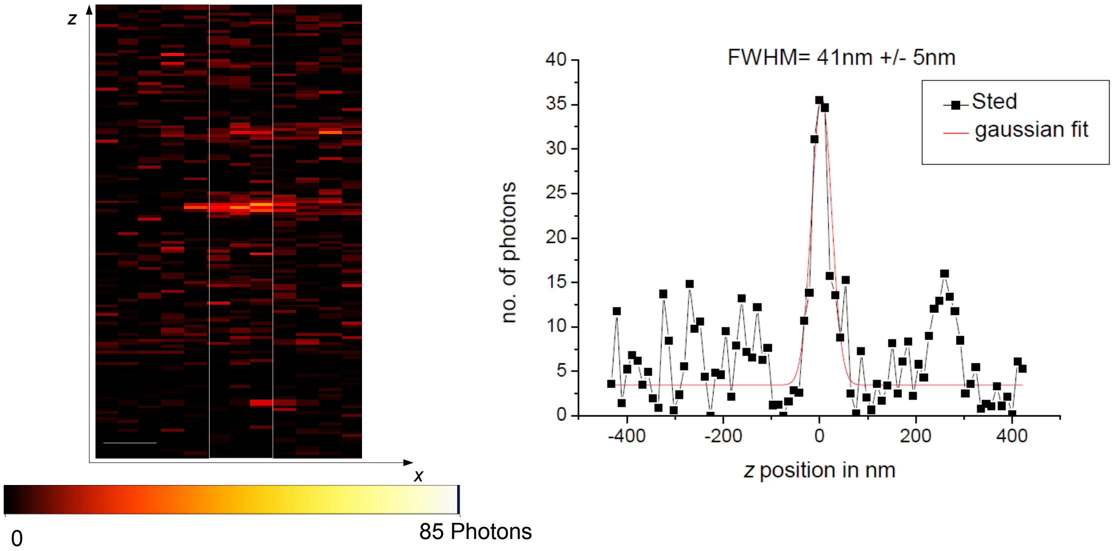

Figure 5.5: Axial 4Pi-STED image of a fluorescent microsphere sample. Image size is 1 µm × 1.7 µm and the scalebar 200 nm. The profile of the indicated area is shown left. The FWHM of the PSF is 41 nm +/- 5 nm. Residual sidelobe signal is negligible.

6

Conclusion and Discussion

In this work the implementation of a 4Pi augmented STED setup parallelized by line illumination is presented. A robust cavity design has been developed and successfully implemented. The parallelization has been achieved by a concept that employs a cylindrical lens for line shaping and an EMCCD for parallel detection. In comparison to Multifocal Microscopy, STED power is used more efficiently, because the illuminated area for the same degree of parallelization is smaller. This means that with the same power of the input pulse a larger area can be imaged without loss of resolution. The parallelization degree with the same power and residual effective volume is increased by a factor of more than four (cf. Fig. A.3). It has to be taken into account here that the resolution along the direction parallel to the line will not be enhanced. This can of course be compensated for by imaging the same area various times while rotating the line in order to superresolve the lacking dimension. Also, it should be noted that the focal volume is already two times smaller than for a standard single lens STED setup. The advantage is that the second superresolved dimension is axial and therefore perpendicular to the image plane or – in other words – the diffraction limited resolution along the line is compensated for by the resolution improvement in axial direction.

Two variants of potential STED PSFs have been considered and the fields have been calculated using the integral approach of Richards and Wolf. The less complex one, the single STED beam approach, uses linear polarized light with polarization parallel to the line in the back focal plane. The advantage is the introduction of a tube like focus with a single beam. However, this approach exhibits a strong dipole dependence, especially in axial direction, where the depleting field is z-polarized. If a sample of randomly orientated, fixed dipoles is considered, this characteristic gives rise to loss of depletion efficiency. In addition the balance between resolution enhancement in lateral direction can not be adapted. Hence, a second approach using two beams and circular polarized light has been considered. For the sake of shaping a tube out of two beams, a polarization dependent phase shift had to be implemented into the cavity. This approach has been successfully implemented by means of four $\lambda/4$-plates in the cavity (cf., Fig. 4.1).

The expected resolution for a sample of randomly oriented, fixed dipole emitters has been calculated. With an available STED power of 230 mW a resolution of 36 nm is predicted for a line of 2.1 μm FWHM for the two beam approach. The expected values for the single beam approach are 26 nm in y- and 95 nm in z-direction.

The line parallelized the scan by a factor of almost ten compared to the size of a lateral confocal PSF of 260 nm. Moreover, line scanning enables a flexible degree of parallelization. This is relevant because the power of the STED beam determines the achievable resolution. Therefore the degree of parallelization trades-off with resolution. However, it has been shown that, when scanning with a line, laser power is used very efficiently and allows a higher degree of parallelization than the multi-spot approach.

For the 4Pi cavity, a completely new design has been chosen to avoid drawbacks of previous setups with respect to stability, accessibility and susceptibility to thermal drift. A rigid mounting frame for the objective lenses has been designed mounted directly on the optical table in contrast to previous designs, in which mounting frames have been attached to the stand of a commercial upright confocal microscope and showed to be prone to vibrations. Brass has been selected as lens mounting frame material to avoid a difference in CTE to the objective lens mechanics made of brass, too. This way the thermal drift due to non-uniform expansion has been minimized. In measurements, drift is low and therefore no re-adjustment has been required during the measurement. This is a significant improvement, since the alignment of 4Pi optics tends to complicate its applicability. The open configuration is superior to previous designs in terms of accessibility and thus facilitates exchange, removal or the fitting of components. This enhancement of flexibility offers a variety of different applications. In addition, alignment issues have been reconsidered and simplified by decoupling most of the alignment axes.

The scanning process and the alignment of tilting of the upper objective lens, the beamsplitter movement and the camera trigger are controlled remotely via a LabVIEW program. It enables hardware control of the galvanometric tilting mirror, the piezoelectric drives, and trigger signal respectively.

A high power titanium sapphire laser has been used for STED depletion. Instead of imaging with a single spot and a three dimensional scan, two dimensional scanning has been carried out with the help of line foci of cylindrical lenses. Images have been acquired with an EMCCD camera.

To qualify the optical performance and to compare it with the calculated results, the PSFs have been visualized with the help of mirror samples, gold colloid samples, and fluorescent microsphere samples. A mirror sample helps to get a rough impression of the PSF shape and helps to validate a number of alignment parameters, namely spherical aberration, decentered beam in the pupil plane and lateral phase plate shift. Therefore, every sample has been prepared on coverslips which are partly vapor deposited with silver. However, since mirror reflections and not the PSF as a response of a point emitter is imaged, it cannot give information about the lateral color error or the quality of the *zero* in axial direction.

Gold colloids scatter the light and allows the qualitative evaluation of the PSF. They are a standard sample in STED alignment and allow to align excitation and STED overlay. A precise quantitative measurement of remaining light in the *zero* is however challenging, since background light components, such as glass reflexes of the sample and any other optical components in the setup. Moreover, gold colloid imaging is restricted to single objective lens measurements, since, in contrast to standard confocal or STED microscopes, in a 4Pi setup a significant part of the incident light is transmitted through the cavity and is redirected back to the detector. This redirected light outshines the scattered light by orders of magnitude.

The signal of a crimson fluorescent microsphere sample, on the other hand, allows to evaluate the PSF of the excitation light. For the STED light, unfortunately, no fluorescent microspheres with suitable excitation spectra were available.

Superresolved STED images of crimson fluorescent microspheres have been acquired. The achieved resolution allows to estimate the STED PSF quality. A resolution about 50 nm and below has been measured for two dimensions.

The predicted resolution of 36 nm could not yet be reached, presumably because of residual aberrations in the beam path and a non perfect *zero* in the center of the STED beam. These misalignment parameters have been analyzed theoretically with respect to their influence on resolution performance. It is primarily affected if the beam is not centered in the pupil plane or if the phase plate is shifted with respect to the beam. An optimal alignment and fluorescent samples that feature improved stability against photo bleaching, should allow to achieve this result.

Since superresolution due to the smaller number of fluorescent probes per effective focal volume comes along with low light signals of the order of 50 counts per second, effective detection is essential. The systems signal-to-noise ratio is determined by the effective dark current and the readout noise of the detector as well as the sample background signal. Characterization of the EMCCD has exhibited an effective readout noise in the order of 0.01 counts per ms for the applied EMCCD gains, yielding a number of 0.1 counts per 10 ms exposure time at 1 MHz readout rate and is thus negligible. It compares to APDs, commonly used in single spot STED system. However, it has been found that the applied hardware binning essentially enhances readout noise. For binning of 4 in one and 10 in the other direction, readout noise increases to values in the order of 0.2 counts per ms. This suggests the use of a more sophisticated determination of the intensity of the ensemble of individual pixels, by data post processing instead of hardware binning, at the cost of acquisition speed. In addition, background signal of samples with dense fluorophores is higher for the line illumination approach, because confocal line detection suppresses background signal less efficient. Out of focus light for line confocal detection scales with 1/z as compared to $1/z^2$ for single spot confocal.

In essence, the setup demonstrates for the first time that the approach of line scanning with circular polarized light is capable of increasing imaging speed of a 4Pi augmented STED with two dimensional superresolution.

7

Outlook

7.1. Extension of superresolution to the third dimension

The line parallelization 4Pi approach has shown a high potential for parallelized three dimensional nanoscopy. Yet, the resolution enhancement was to this point restricted to two dimensions. To include the missing dimension – the resolution parallel to the line – the line focus has to be rotated. A beam can be rotated with the help of an odd number of reflections in a K-mirror (cf. Fig. 7.1) [72].

Depolarization can be minimized using mirror reflections instead of Abbe-König prisms [73], that employ, in principle, the same arrangement, but do use total internal reflection on glass surfaces, that gives rise to depolarization.

These optics are standard in confocal microscopy, however, their alignment is elaborate and has not been accomplished here.

7.2. RESOLFT with switchable proteins

The field of view in line scanning microscopy is in principle the same as for single point scanning. However for STED available power limits the degree of parallelization.

Therefore, RESOLFT methods that need less laser power are of interest. The states of molecular switches, such as proteins, can be controlled with laser powers

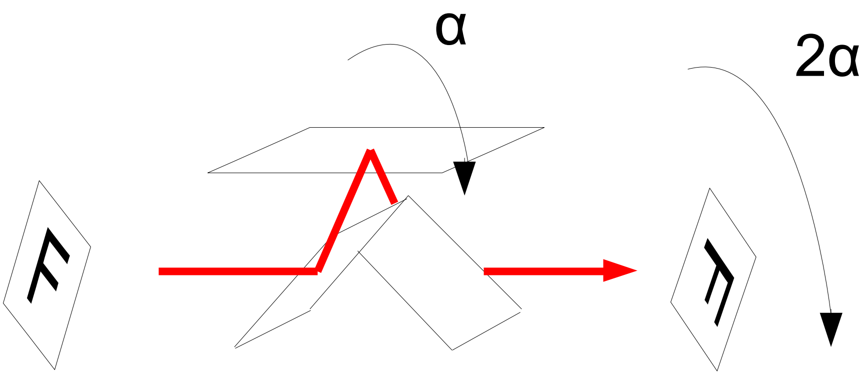

Figure 7.1: A K-mirror enables image rotation. The underlying principle is the odd number of reflections in a common rotating element as shown. A K-mirror consists of a plane mirror and a silver coated prism. However, due to the odd number of reflections, the image is mirror-inverted with respect to the plane parallel to the top mirror. As the device is rotated, this leads to an image rotation. The rotation angle of the image is twice the rotation angle of the device.

that are in the order of 10^6 times smaller than typical STED powers. Besides practical aspects, low-intensity illumination – especially in living samples – is desirable to minimize the light exposure to the sample.

The process is no longer power limited, but rather limited by the number of switching cycles a molecule can undergo before it becomes photo-bleached. Here a line or a line pattern can reduce the number of switching cycles. The methods developed in this work may be fundamental in this field, since recent research progress has been made in low-intensity RESOLFT methods, that employ certain proteins which can be switched between a fluorescent and a non fluorescent state several 100 to 1000 times [74], [11].

A number of such proteins have been generated [75], [76] of which the most suitable for RESOLFT so far are Dronpa, and dedicated rsEGFPs. Those proteins are mutants of GFP [77], that have been designed to show reversible switching behaviour when exposed to light of certain wavelengths. A switching measurement (cf., Fig 7.2) has been carried out by sequentially exposing a sample of E.Colis filled with rs EGFP with light of 405 nm for on-switching and with 470 nm for off-switching and excitation. Switching times are on the order of milliseconds. As a consequence,

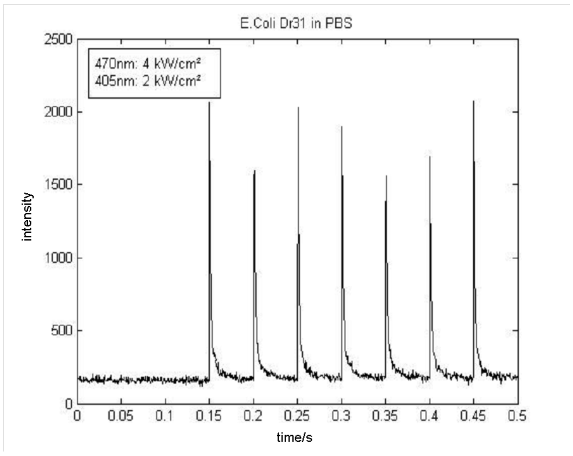

Figure 7.2: Switching measurement of reversible switchable proteins Dronpa, expressed in E.Coli. The switching times are is on the order of milliseconds and switching powers are orders of magnitude smaller than for STED.

compared to STED much lower average laser intensities are needed for the switching process, because it is no longer necessary to compete with the fluorescent lifetime of only a few nanoseconds. However, these longer switching times slow down the acquisition process. Thus, parallelization becomes even more important. Additionally, the number of switching in cycles – that is limited to 100 to 1000 – is reduced when scanning with a line.

Recently a new protein called Dreiklang [78] has been found that is capable of performing switching at wavelength other than the excitation wavelength. This means, that the excitation for readout no longer effects the on/off-states of the protein. This is an important improvement over previous proteins, that are switched off during imaging.

Ongoing experiments will reveal which imaging speed and degree of parallelization is optimal for RESOLFT with switchable proteins. The developed methods, presented in this work may be used for any RESOLFT type method including the use of optically switchable proteins in the future.

A

Appendix

A.1. PSF calculations

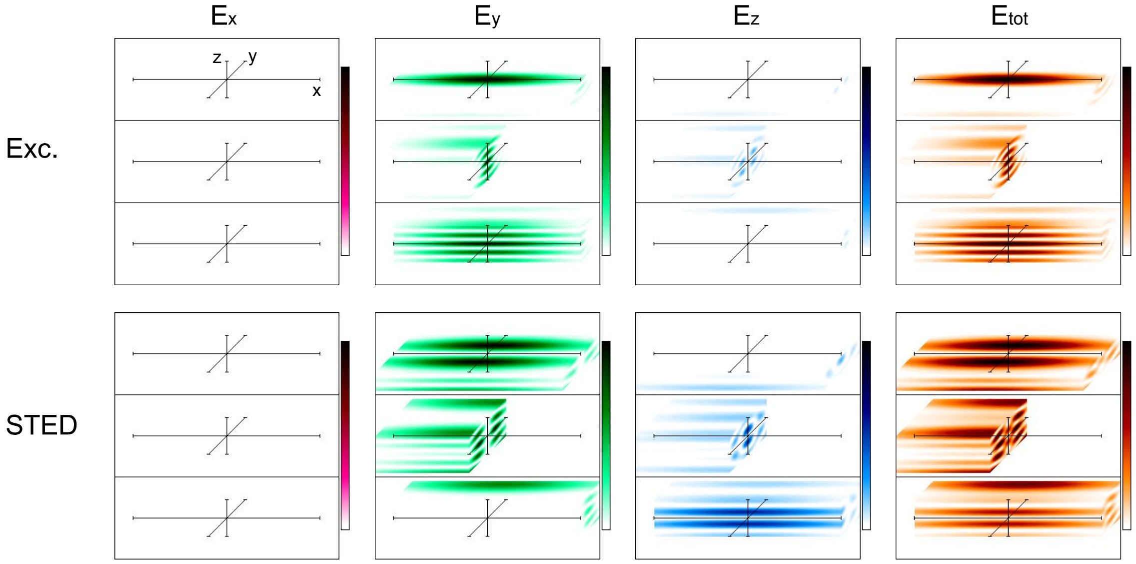

Figure A.1: PSFs of the single-beam approach. The upper row shows the excitation. the second row the STED. Polarization components are shown in magenta (x-polarization), green (y-polarization), and blue (z-polarization).

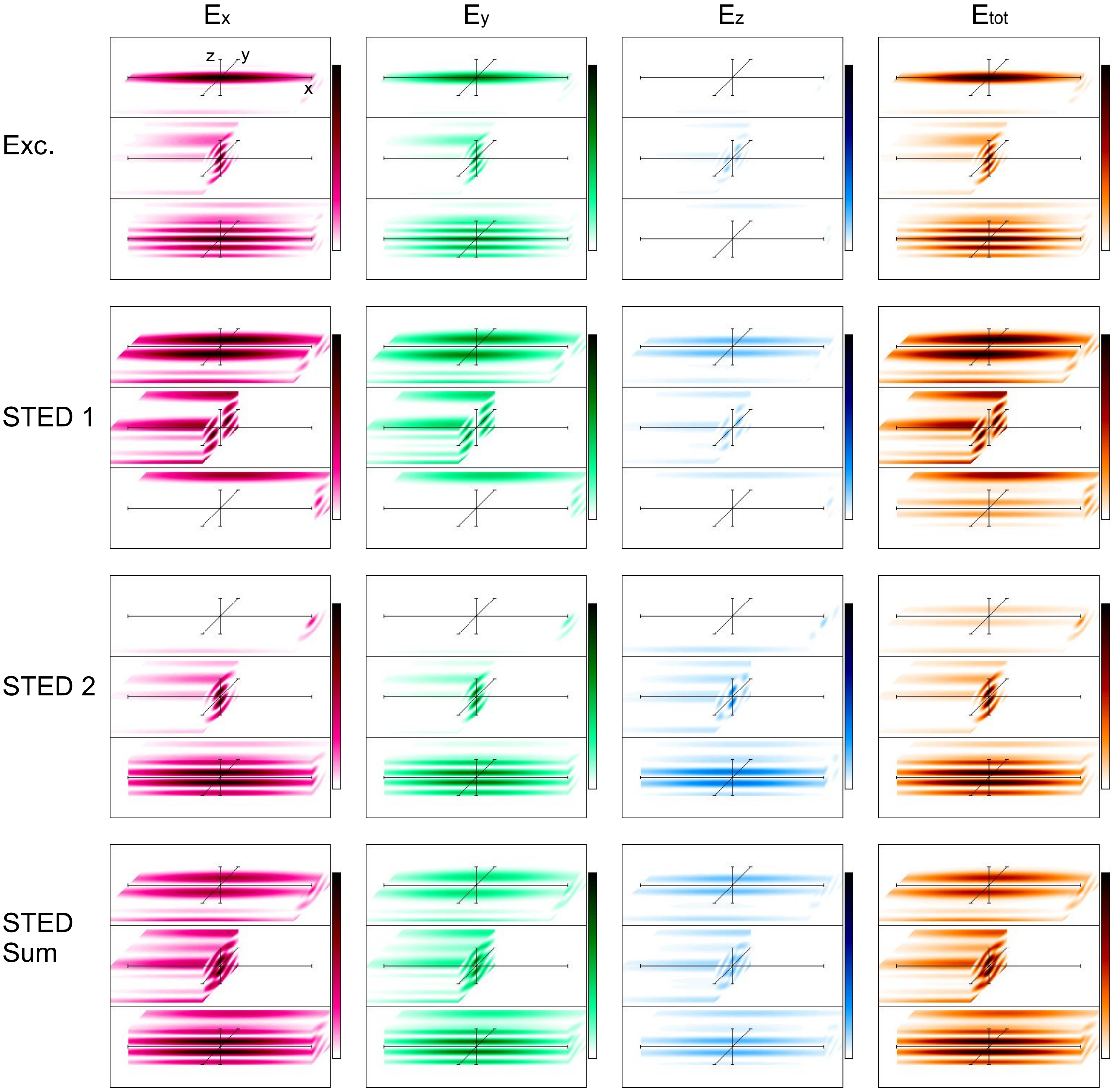

Figure A.2: PSFs of the two-beam approach. The upper row shows the excitation. the second row the STED beam for lateral and the third row the STED beam for axial resolution enhancement. The last row shows the sum of the two STED beams. Polarization components are shown in magenta x-polarization, green y-polarization, and blue z-polarization.

A.2. Laser power balance for resolution calculations

Line length in μm	FWHM in back aperture in μm	Power of beam 1 in mW	Power of beam 2 in mW	Focal FWHM of y and z in nm
0.26	4000	182.0	48	20
1.40	400	184.0	46.0	27
2.10	200	186.0	44.0	36
3.70	150	187.0	43.0	40
5.60	100	189.0	41.0	48
7.50	75	192.5	37.5	54
9.40	60	195.0	35.0	60
11.30	50	197.3	32.7	65
14.30	40	201.5	28.5	71
16.70	35	203.5	26.5	74
21.00	30	204.0	26.0	77

Table A.1: Parameters for the resolution calculations. STED power for the two beams has been balanced so that the FWHM for y- and z-direction is equal. Total STED power is 230 mW. FLuorescent probes of 20 nm have been assumed.

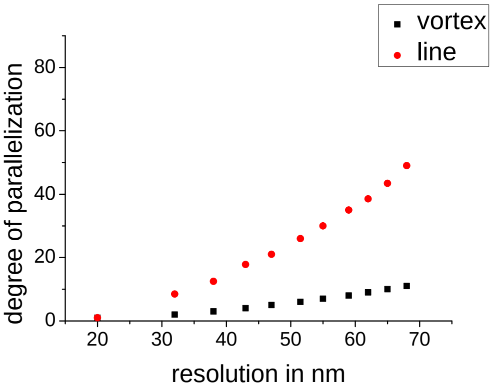

Figure A.3: Degree of parallelization he 4Pi two-beam approach (caption line) in comparison to a single lens STED performance with multiple STED beams, employing a vortex phase plate. 230 mW, 765 nm available laser power have been assumed.

A.3. Consideration of the transmitted light in the 4Pi cavity

If quarter-wave plates are inserted in the demonstrated manner, the two outputs of the Sagnac type cavity are inverted. This can be comprehended mathematically by means of the Jones Matrices.

in	first quater waveplate	second quater waveplate	third quater waveplate	fourth quater waveplate	out
$\begin{pmatrix}1\\0\end{pmatrix}$	$e^{\frac{\pi}{4}\cdot i}\begin{pmatrix}1 & 0\\0 & i\end{pmatrix}$	$\frac{e^{-\frac{\pi}{4}\cdot i}}{\sqrt{2}}\cdot\begin{pmatrix}i & 1\\1 & i\end{pmatrix}$	$\frac{e^{-\frac{\pi}{4}\cdot i}}{\sqrt{2}}\cdot\begin{pmatrix}i & 1\\1 & i\end{pmatrix}$	$e^{\frac{\pi}{4}\cdot i}\begin{pmatrix}1 & 0\\0 & -i\end{pmatrix}$	$\begin{pmatrix}0\\1\end{pmatrix}$
$\begin{pmatrix}1\\0\end{pmatrix}$	$e^{\frac{\pi}{4}\cdot i}\begin{pmatrix}1 & 0\\0 & -i\end{pmatrix}$	$\frac{e^{\frac{\pi}{4}\cdot i}}{\sqrt{2}}\cdot\begin{pmatrix}1 & i\\i & 1\end{pmatrix}$	$\frac{e^{\frac{\pi}{4}\cdot i}}{\sqrt{2}}\cdot\begin{pmatrix}1 & i\\i & 1\end{pmatrix}$	$e^{\frac{\pi}{4}\cdot i}\begin{pmatrix}1 & 0\\0 & i\end{pmatrix}$	$e^{\pi}\cdot\begin{pmatrix}0\\1\end{pmatrix}$
$\begin{pmatrix}0\\1\end{pmatrix}$	$e^{\frac{\pi}{4}\cdot i}\begin{pmatrix}1 & 0\\0 & i\end{pmatrix}$	$\frac{e^{-\frac{\pi}{4}\cdot i}}{\sqrt{2}}\cdot\begin{pmatrix}i & 1\\1 & i\end{pmatrix}$	$\frac{e^{-\frac{\pi}{4}\cdot i}}{\sqrt{2}}\cdot\begin{pmatrix}i & 1\\1 & i\end{pmatrix}$	$e^{\frac{\pi}{4}\cdot i}\begin{pmatrix}1 & 0\\0 & -i\end{pmatrix}$	$\begin{pmatrix}1\\0\end{pmatrix}$
$\begin{pmatrix}0\\1\end{pmatrix}$	$e^{\frac{\pi}{4}\cdot i}\begin{pmatrix}1 & 0\\0 & -i\end{pmatrix}$	$\frac{e^{\frac{\pi}{4}\cdot i}}{\sqrt{2}}\cdot\begin{pmatrix}1 & i\\i & 1\end{pmatrix}$	$\frac{e^{\frac{\pi}{4}\cdot i}}{\sqrt{2}}\cdot\begin{pmatrix}1 & i\\i & 1\end{pmatrix}$	$e^{\frac{\pi}{4}\cdot i}\begin{pmatrix}1 & 0\\0 & i\end{pmatrix}$	$e^{\pi}\cdot\begin{pmatrix}1\\0\end{pmatrix}$

Table A.2: Jones vectors and matrices for the two polarization state of the transmitted beams. The counter-propagating beams pass the waveplates in opposing order and the angle is mirrored. Therefore the matrices for the second and third quarter-wave plates where calculated for an angle of 45° and -45°, respectively.

A.4. Preparation of gold colloid and fluorescent microsphere samples

In order to facilitate 4Pi alignment customized coverslips of 30 mm diameter and 150 mm thickness have been used. One quadrant of the surface was silver coated at the optics workshop of the MPIbpc in Göttingen, Germany by vapor deposition. It has been used as alignment aid (cf. section 4.4 and 5.1). The remaining glass surface has been used for sample preparation. A 200 µl drop of poly-l-lysine has been incubated for 5 minutes on the slip and washed with distilled water. A dilution of microspheres or colloids (1:10000 dilution of Fluoropheres Carboxylate-Modified Microspheres, diameter 20 nanometer, Crimson Fluorescent 2% solids or 1:2 dilution of gold colloid BBI international, 40nm) in milliQ water has been prepared and a 200 µl drop of this dilution has been incubated for 15 minutes and washed again. A drop of 97% (v/v) 2,2'-Thiodiethanol (TDE) (refractive index n = 1.515 at room temperature) has been placed on the middle of the surface and covered with a second black coverslip. This procedure has to be done carefully, so that no air bubbles are enclosed. The sample has been sealed with nail polish.

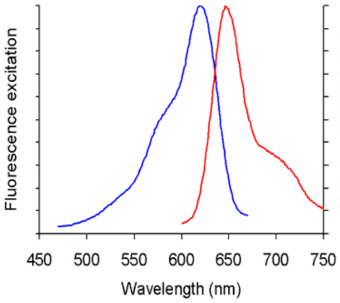

Figure A.4: Excitation (blue) and emission (red) spectra of crimson fluorescent microspheres [79].

A.5. Camera settings and characteristics

The camera has been set to "run till abort" acquisition mode, image readout mode. The acquisition has been triggered externally with the help of a Labview controlled signal to permit a handshake with the scanning process. The temperature of the CCD was -90°. Hardware binning of 4×10 was applied.

EM Gain	Hardware Binning	5-σ filtered readout noise in no. of electrons	5-σ filtered readout noise in no. of photons
5	1×1	2.00	2.30
10	1×1	2.03	1.16
30	1×1	2.11	0.42
100	1×1	2.18	0.13
260	1×1	2.21	0.12
300	1×1	2.27	0.05
1,346	1×1	2.26	0.07
5	4×10	2.50	3.00
10	4×10	3.10	1.80
30	4×10	7.90	1.50
100	4×10	26.00	1.60
265	4×10	53.00	2.00
300	4×10	74.00	1.30
1,346	4×10	196.00	1.80

Table A.3: Camera characteristics for different EM gain settings. The readout noise increases significantly if hardware binning is applied.

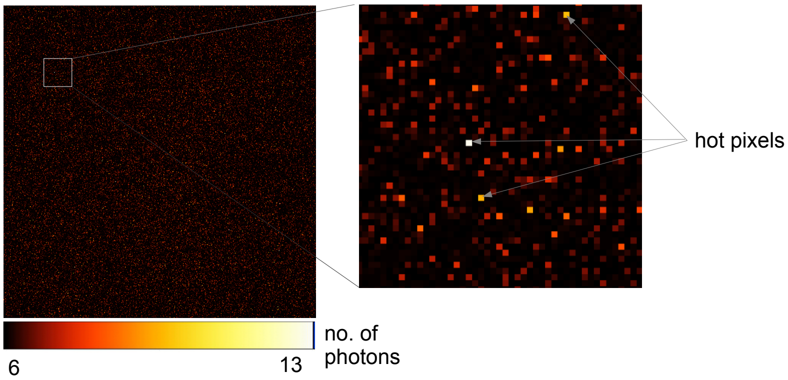

Figure A.5: Background image of the EMCCD 512 × 512 Pixels taken at 1346 EM gain and 10 Mhz readout speed, 10 ms exposure time with. 2% of the pixels have values above 5 σ and should be considered outliers. If hardware binning is applied, they give rise to excess noise.

Bibliography

[1] E. Abbe. Beiträge zur Theorie des Mikroskops und der mikroskopischen Wahrnehmung. *Archiv für Mikroskopische Anatomie*, 9:413–468, 1873.

[2] M. Fernandez-Suarez and A. Y. Ting. Fluorescent probes for super-resolution imaging in living cells. *Nature Reviews Molecular Cell Biology*, 9:929–943, 2008.

[3] E. Betzig, G. H. Patterson, R. Sougrat, O. W. Lindwasser, S. Olenych, J. S. Bonifacino, M. W. Davidson, J. Lippincott-Schwartz, and H. F. Hess. Imaging intracellular fluorescent proteins at nanometer resolution. *Science*, 313(5793):1642–1645, 2006.

[4] S. T. Hess, T. P. K. Girirajan, and M. D. Mason. Ultra-high resolution imaging by fluorescence photoactivation localization microscopy. *Biophysical Journal*, 91(11):4258–4272, 2006.

[5] M. J. Rust, M. Bates, and X. W. Zhuang. Sub-diffraction-limit imaging by stochastic optical reconstruction microscopy (storm). *Nature Methods*, 3:793–795, 2006.

[6] M. Heilemann, S. van de Linde, M. Schuttpelz, R. Kasper, B. Seefeldt, A. Mukherjee, P. Tinnefeld, and M. Sauer. Subdiffraction-resolution fluorescence imaging with conventional fluorescent probes. *Angewandte Chemie (international edition)*, 47:6172–6176, 2008.

[7] A. Sharonov and R. M. Hochstrasser. Wide-field subdiffraction imaging by accumulated binding of diffusing probes. *Proceedings of the National Academy of Sciences of the United States of America*, 103(50):18911–18916, 2006.

[8] J. Fölling, M. Bossi, H. Bock, R. Medda, C. A. Wurm, B. Hein, S. Jakobs, C. Eggeling, and S. W. Hell. Fluorescence nanoscopy by ground-state depletion and single-molecule return. *Nature Methods*, 5:943–945, 2008.

[9] M. A. Schwentker, H. Bock, M. Hofmann, S. Jakobs, J. Bewersdorf, C. Eggeling, and S. W. Hell. Wide-field subdiffraction resolft microscopy using fluorescent protein photoswitching. *Microscopy Research and Technique*, 70(3):269–280, 2007.

[10] M. Hofmann, C. Eggeling, S. Jakobs, and S. W. Hell. Breaking the diffraction barrier in fluorescence microscopy at low light intensities by using reversibly photoswitchable proteins. *Proceedings of the National Academy of Sciences of the United States of America*, 102(49):17565–17569, 2005.

[11] T. Grotjohann, I. Testa, M. Leutenegger, C. Eggeling, S. Hell, and S. Jakobs. Reversibly switchable enhanced green fluorescent protein (rsegfp): a novel photochromic fluorescent protein enables resolft-type microscopy of living cells at low light intensities. *Protein Science*, 21:163–163, August 2012.

[12] A. C. Stiel, M. Andresen, H. Bock, M. Hilbert, J. Schilde, A. Schonle, C. Eggeling, A. Egner, S. W. Hell, and S. Jakobs. Generation of monomeric reversibly switchable red fluorescent proteins for far-field fluorescence nanoscopy. *Biophysical Journal*, 95:2989–2997, 2008.

[13] M. Bossi, V. Belov, S. Polyakova, and S. W. Hell. Reversible red fluorescent molecular switches. *Angewandte Chemie (international Edition)*, 45(44):7462–7465, 2006.

[14] S.W. Hell and M. Kroug. Ground-state depletion fluorescence microscopy, a concept for breaking the diffraction resolution limit. *Applied Physics B: Lasers and Optics*, 60:495–497, 1995.

[15] S.W. Hell and J. Wichmann. Breaking the diffraction resolution limit by stimulated-emission - stimulated-emission-depletion fluorescence microscopy. *Optics Letters*, 19(11):780–782, 1994.

[16] E. Rittweger, K. Y. Han, S. E. Irvine, C. Eggeling, and S. W. Hell. Sted microscopy reveals crystal colour centres with nanometric resolution. *Nature Photonics*, 3:144–147, 2009.

[17] G. Donnert, J. Keller, R. Medda, M. A. Andrei, S. O. Rizzoli, R. Lurmann, R. Jahn, C. Eggeling, and S. W. Hell. Macromolecular-scale resolution in biological fluorescence microscopy. *Proceedings of the National Academy of Sciences of the United States of America*, 103(31):11440–11445, 2006.

[18] V. Westphal, S. O. Rizzoli, M. A. Lauterbach, D. Kamin, R. Jahn, and S. W. Hell. Video-rate far-field optical nanoscopy dissects synaptic vesicle movement. *Science*, 320(5873):246–249, 2008.

[19] B. Hein, K. I. Willig, and S. W. Hell. Stimulated emission depletion (sted) nanoscopy of a fluorescent protein-labeled organelle inside a living cell. *Proceedings of the National Academy of Sciences of the United States of America*, 105(38):14271–14276, 2008.

[20] U. V. Nagerl, K. I. Willig, B. Hein, S. W. Hell, and T. Bonhoeffer. Live-cell imaging of dendritic spines by sted microscopy. *Proceedings of the National Academy of Sciences of the United States of America*, 105:18982–18987, 2008.

[21] J.B. Ding, K.T. Takasaki, and B.L. Sabatini. Supraresolution imaging in brain slices using stimulated-emission depletion two-photon laser scanning microscopy. *Neuron*, 63:429–437, 2009.

[22] Nicolai T. Urban, Katrin I. Willig, Stefan W. Hell, and U. Valentin Nägerl. Sted nanoscopy of actin dynamics in synapses deep inside living brain slices. *Biophysical Journal*, 101(5):1277 – 1284, 2011.

[23] Sebastian Berning, Katrin I. Willig, Heinz Steffens, Payam Dibaj, and Stefan W. Hell. Nanoscopy in a living mouse brain. *Science*, 335:551, 2012.

[24] K. Y. Han, K. I. Willig, E. Rittweger, F. Jelezko, C. Eggeling, and S. W. Hell. Three-dimensional stimulated emission depletion microscopy of nitrogen-vacancy centers in diamond using continuous-wave light. *Nano Letters*, 9(9):3323–3329, 2009.

[25] B. Harke, C. K. Ullal, J. Keller, and S. W. Hell. Three-dimensional nanoscopy of colloidal crystals. *Nano Letters*, 8(5):1309–1313, 2008.

[26] M. C. Lang, T. Staudt, J. Engelhardt, and S. W. Hell. 4pi microscopy with negligible sidelobes. *New Journal of Physics*, 10:1–13, 2008.

[27] M. Dyba. *STED-4Pi microscopy*. PhD thesis, 2004.

[28] M. Dyba and S. W. Hell. Focal spots of size lambda/23 open up far-field florescence microscopy at 33 nm axial resolution. *Physical Review Letters*, 88(16):163901, 2002.

[29] R. Schmidt, C. A. Wurm, S. Jakobs, J. Engelhardt, A. Egner, and S. W. Hell. Spherical nanosized focal spot unravels the interior of cells. *Nature Methods*, 5(6):539–544, 2008.

[30] Daniel Aquino, Andreas Schonle, Claudia Geisler, Claas v Middendorff, Christian A Wurm, Yosuke Okamura, Thorsten Lang, Stefan W Hell, and Alexander Egner. Two-color nanoscopy of three-dimensional volumes by 4pi detection of stochastically switched fluorophores. *Natural Immunity Methods*, 8(4):353 – 359, April 2011.

[31] G. Shtengel, J. A. Galbraith, C. G. Galbraith, J. Lippincott-Schwartz, J. M. Gillette, S. Manley, R. Sougrat, C. M. Waterman, P. Kanchanawong, M. W.

Davidson, R. D. Fetter, and H. F. Hess. Interferometric fluorescent super-resolution microscopy resolves 3d cellular ultrastructure. *Proceedings of the National Academy of Sciences of the United States of America*, 106(9):3125–3130, 2009.

[32] Pit Bingen, Matthias Reuss, Johann Engelhardt, and Stefan W. Hell. Parallelized sted fluorescence nanoscopy. *Optics Express*, 19(24):23716 – 26, 2011.

[33] A. Egner and S. W. Hell. Time multiplexing and parallelization in multifocal multiphoton microscopy. *Optical Society of America. Journal A: Optics, Image Science, and Vision*, 17:1192–1201, 2000.

[34] Dorothea Sauter. *4Pi live cell imaging.* PhD thesis, 2009.

[35] M. Born and E. Wolf. *Principles of Optics.* Pergamon Press, Oxford, 6th edition, 1993.

[36] J. B. Pawley. *Handbook of biological confocal microscopy.* Springer, New York, 2nd edition, 2006.

[37] L. Novotny and B. Hecht. *Principles of nano-optics.* Cambridge University Press, Cambridge, 2006.

[38] J. W. Rayleigh. On the theory of optical images, with special reference to the microscope. *Philosophical Magazine*, 5(42):167 – 195, 1896.

[39] E. Verdet. *Lessons d' optique physique*, volume 1. Victor Masson et fils, Paris, 1869.

[40] J. W. Rayleigh. On the manufacture and theory of diffraction-gratings. *Philosophical Magazine*, 47(310):81 – 93, 1874.

[41] S.W. Hell. Double-scanning confocal microscope european patent, 1992.

[42] A. Egner and S. W. Hell. Fluorescence microscopy with super-resolved optical sections. *Trends in Cell Biology*, 15(4):207–215, 2005.

[43] A. Egner, S. Jakobs, and S. W. Hell. Fast 100-nm resolution three-dimensional microscope reveals structural plasticity of mitochondria in live yeast. *Proceedings of the National Academy of Sciences of the United States of America*, 99:3370–3375, 2002.

[44] A. Egner, S. Verrier, A. Goroshkov, H. D. Soling, and S. W. Hell. 4pi-microscopy of the golgi apparatus in live mammalian cells. *Journal of Structural Biology*, 147(1):70–76, 2004.

[45] S.W. Hell, S. Lindek, C. Cremer, and E. H. K. Stelzer. Measurement of the 4pi-confocal point spread function proves 75 nm resolution. *Applied Physics Letters*, 64(11):1335–1338, 1994.

[46] S.W. Hell, S. Lindek, and E. H. K. Stelzer. Enhancing the axial resolution in far-field light microscopy: two-photon excitation 4pi-confocal fluorescence microscopy. *Journal of Modern Optics*, 41(4):675–681, 1994.

[47] B. Richards and E. Wolf. Electromagnetic diffraction in optical systems .2. structure of the image field in an aplanatic system. *Royal Society of London. Proceedings. Mathematical and Physical Sciences*, 253:358–379, 1959.

[48] A. Egner, V. Andresen, and S. W. Hell. Comparison of the axial resolution of practical nipkow-disk confocal fluorescence microscopy with that of multifocal multiphoton microscopy: Theory and experiment. *Journal of Microscopy*, 206:24 – 32, 2002.

[49] T. A. Klar and S. W. Hell. Subdiffraction resolution in far-field fluorescence microscopy. *Optics Letters*, 24(14):954–956, 1999.

[50] S.W. Hell. Microscopy and its focal switch. *Nature Methods*, 6(1):24–32, 2009.

[51] S.W. Hell. Far-field optical nanoscopy. *Science*, 316(5828):1153–1158, 2007.

[52] S. Hell. *Far-Field Optical Nanoscopy*, pages 365 – 398. Springer, Berlin, 2009.

[53] B. Harke, J. Keller, C. K. Ullal, V. Westphal, A. Schoenle, and S. W. Hell. Resolution scaling in sted microscopy. *Optics Express*, 16(6):4154–4162, 2008.

[54] K. I. Willig, B. Harke, R. Medda, and S. W. Hell. Sted microscopy with continuous wave beams. *Nature Methods*, 4(11):915–918, 2007.

[55] T. Zuchner, A. V. Failla, and A. J. Meixner. Light microscopy with doughnut modes: A concept to detect, characterize, and manipulate individual nanoobjects. *Angewandte Chemie-international Edition*, 50(23):5274–5293, 2011.

[56] http://learn.hamamatsu.com/articles/photomultipliers.html. Last accessed on 2012-24-20.

[57] http://learn.hamamatsu.com/articles/avalanche.html. Last accessed on 2012-24-20.

[58] http://learn.hamamatsu.com/articles/emccds.html. Last accessed on 2012-24-20.

[59] J. Bewersdorf and S. W. Hell. Picosecond pulsed two-photon imaging with repetition rates of 200 and 400 mhz. *Journal of Microscopy*, 191:28–38, 1998.

[60] A. Deniset-Besseau, S. Leveque-Fort, M. P. Fontaine-Aupart, G. Roger, and P. Georges. Three-dimensional time-resolved fluorescence imaging by multifocal multiphoton microscopy for a photosensitizer study in living cells. *Appl. Opt.*, 46(33):8045–8051, Nov 2007.

[61] Matthias Fricke and Tim Nielsen. Two-dimensional imaging without scanning by multifocal multiphoton microscopy. *Appl. Opt.*, 44(15):2984–2988, May 2005.

[62] T. E. Keller, M. H. Rubin, and Y. H. Shih. Three-photon entangled state fortschritte der physik-progress of physics. volume 46, pages 673–682.

[63] K. Fujita, O. Nakamura, T. Kaneko, M. Oyamada, T. Takamatsu, and S. Kawata. Confocal multipoint multiphoton excitation microscope with microlens and pinhole arrays. *Optics Communications*, 174:7–12, 2000.

[64] M. Straub, P. Lodemann, P. Holroyd, R. Jahn, and S. W. Hell. Live cell imaging by multifocal multiphoton microscopy. *European Journal of Cell Biology*, 79:726–734, 2000.

[65] Jan Keller. *Optimal de-excitation patterns for RESOLFT-Microscopy*. na, 2006.

[66] Matthias Reuss. Simpler sted setups, 2010.

[67] M. Reuss, J. Engelhardt, and S. W. Hell. Birefringent device converts a standard scanning microscope into a sted microscope that also maps molecular orientation. *Optics Express*, 18(2):1049 – 1058, 2010.

[68] M. Lang, T. Muller, J. Engelhardt, and S. W. Hell. 4pi microscopy of type a with 1-photon excitation in biological fluorescence imaging. *Optics Express*, 15(5):2459–2467, 2007.

[69] D. Mende G. Simon. *Physik Gleichungen und Tabellen*, volume 6. VEB Fachbuchverlag Leipzig, 1975.

[70] Y. Cheng R. Li S. Deng, L. Liu and Z. Xu. Effects of primary aberrations on the fluorescence depletion patterns of sted microscopy. *Optics Express*, 18:1657 – 1666, 2010.

[71] Pit Bingen. *Parallelised STED nanoscopy*. PhD thesis, University of Heidelberg, 2012.

[72] R.H. Hildebrand. Focal plane optics in far-infrared and submillimeter astronomy. *Optical Engineering*, 25:323 – 330, 1986.

[73] William L. Wolfe. *Handbook of optics, No. 2: Devices, Measurements, and Properties.*, chapter Nondispersive Prisms, pages 4 – 8. McGraw-Hill, 1995.

[74] Ilaria Testa, Nicolai T. Urban, Stefan Jakobs, Christian Eggeling, Katrin I. Willig, and Stefan W. Hell. Nanoscopy of living brain slices with low light levels. *Neuron*, 75(6):992 – 1000, 2012.

[75] M. Andresen, M. C. Wahl, A. C. Stiel, F. Grater, L. V. Schafer, S. Trowitzsch, G. Weber, C. Eggeling, H. Grubmuller, S. W. Hell, and S. Jakobs. Structure and mechanism of the reversible photoswitch of a fluorescent protein. *Proceedings of the National Academy of Sciences of the United States of America*, 102(37):13070–13074, 2005.

[76] R. A. G. Cinelli, V. Pellegrini, A. Ferrari, P. Faraci, R. Nifosi, M. Tyagi, M. Giacca, and F. Beltram. Green fluorescent proteins as optically controllable elements in bioelectronics. *Applied Physics Letters*, 79(20):3353–3355, 2001.

[77] R. Y. Tsien and A. Waggoner. *Fluorophores for confocal microscopy*, pages 267–279. Plenum Press, New York, 1995.

[78] T. Brakemann, A. C. Stiel, G. Weber, M. Andresen, I. Testa, T. Grotjohann, M. Leutenegger, U. Plessmann, H. Urlaub, C. Eggeling, M. C. Wahl, S. W. Hell, and S. Jakobs. A reversibly photoswitchable gfp-like protein with fluorescence excitation decoupled from switching. *Nature Biotechnology*, 29(10):942–U132, October 2011.

[79] http://products.invitrogen.com/ivgn/product/F8782. Last accessed on 2012-24-20.

List of Acronyms

AFM	Atomic Force Microscopy
APD	Avalanche PhotoDiode
CAD	Computer-Aided Design
CCD	Charged Coupled Device
CTE	Coefficient of Thermal Expansion
CW	Continuous Wave
DAC	Digital Analogue Converter
EGFP	Coefficient of Thermal Expansion
EGFP	Enhanced Green Fluorescent Protein
EMCCD	Electron Multiplying Charged Coupled Device
FWHM	Full Width at Half Maximum
GFP	Green Fluorescent Protein
GSDim	Ground State Depletion followed by Individual Molecule return
MMM	Multifocal Multiphoton Microscopy
MPIbpc	Max Planck Institute for biophysical chemistry
PAINT	Point Accumulation for Imaging in Nanoscale Topography
PALM	Photo Activated Localization Microscopy
PBS	Polarizing Beam Splitter
PCI	Peripheral Component Interconnect
PMT	PhotoMultiplier Tube
PSF	Point Spread Function

RESOLFT	REversible Saturable OpticaL Fluorescence Transitions
SNOM	Scanning Near field Optical Microscopy
SNR	Signal-to-Noise Ratio
STED	STimulated Emission Depletion
STORM	STochastic Optical Reconstruction Microscopy

List of Figures

Acknowledgements

I want to acknowledge all the people who helped me to accomplish this work. Thanks to my supervisor Stefan W. Hell at MPI Göttingen who gave me the possibility to work in his group at the German Cancer Research Center in Heidelberg and to present my work in several international conferences. Thanks to Wolfgang Petrich, who agreed to be second referee.

For the idea of my project, guidance and motivation I want to thank Johann Engelhardt. Without his experience and ideas, this work would not have been possible. He was an enormous source of inspiration and motivation. Also, I was lucky to find a good working atmosphere in our laboratory. Especially Dorothea Sauter and Thorsten Staudt helped me to get started with the setup. Thanks for your helpfulness and kindness: Eva Rittweger, Patrick Hoyer, Pit Bingen, Jale Schneider, Jasmin Zahn, Matthias Henrich, Matthias Reuss, Frederick Görlitz, Nikolas Dimitriadis, Daniel Aquino, Dörte Oltmanns, Konrad Beyer, Marlina Hoffmann, Andreas Engler, Susanne Schrof, Christoph Muus, Lucas Alber, Florian Heigwer and all the interns. Thanks to my colleges in Göttingen, especially Roman Schmidt, Hannes Bock, Tim Grotjohann, Ilaria Testa and Stefan Jakobs.

For the machining of the cavity parts and hints on construction, I want to acknowledge the work shop of Heinrich Rühle and his team at the German Cancer Research Center. Especially Wolfram Stroh contributed immensely on the successful assembling of the objective lens attachment. Thank you for your effort and interest in my project. Thanks to the electronic work shop for the circuit boards.

Thanks for proof-reading: Johann Engelhardt, my family, Imke Diddens and Jasmin Vural. Special thanks to the BioQuant girls for all the fun moments we shared – not only at laboratory: Dorothea Sauter, Christina Spassova, Jasmin Zahn, Jale Schneider, Eva Rittweger, Jessica Balbo. Thank you, Khaled, for your catching optimism and love.

Finally, I want to thank my family for their love, generosity and support beyond compare.